



POLITECNICO DI TORINO

Master degree course in Nanotechnology for ICTs

Master Degree Thesis

**Magnetic MRAM memory and
magnetic field sensor:
multi-functionality for 3D assembly**

Supervisor

Prof. Carlo RICCIARDI

Candidate

Leonardo FIORENTINI
matricola s265639

Internship Tutor

Dott. Ricardo SOUSA

GRADUATION SESSION - OCTOBER 2020

This work is subject to the Creative Commons Licence

Summary

In the last few years, people are moving from planar technology to 3D integration, this is due to the fact that the latter has lower production costs, higher versatility and the final device is more compact. 3D integration consists into stacking wafers one on top to the other; to this end a very problematic issue is wafers misalignment. When wafers aren't well aligned we can have, in the worst case, diffusion of Copper into Silicon Dioxide; anyway, the lower is the surface area bonded and the lower is the current that can pass through the device we want to assemble, breaking down its efficiency. To do so, a system based on a magnetic element and a magnetic sensor is incorporated in the wafers to be bond. In this project a magnetic STT-MRAM is used as magnetic sensor in order to detect possible misalignment in the vertical and horizontal directions.

The STT-MRAM is a device that is able to have two possible resistance states, an high resistance state and a low resistance state; it is possible to switch the device from one state to the other, either by applying a voltage pulse or by applying a magnetic field. If a magnetic field is applied, the voltage pulse, that allows the transition, changes in magnitude. This change is linear and allows us to exploits this behaviour in order to be able to detect the field applied by having a certain switching voltage as output. The work is split in two main parts: the simulation part and the experimental part. In the simulation part we will study the critical parameters and we will see the role of the voltage dispersion. The voltage dispersion is responsible of the resolution of the sensor, indeed, we will see that the higher is the voltage dispersion and the lower is the accuracy in the determination of the magnetic field for a given switching voltage. Then, we will study how the voltage dispersion will influence the TMR (Tunnel Magnetic Resistance). After, we'll move on with the simulation of the magnetic element (or marker) and we'll see the behaviour of the sensor with the non-uniform field generated by the marker. Then, we will study the vertical and lateral sensitivity for displacements detection, both in horizontal and in vertical direction; further, we will analyse different geometries in order to improve these two magnitudes. In the experimental part we'll show the linear behaviour of the switching voltage and we'll provide a study of the voltage dispersion.

Contents

1	Introduction	5
1.1	Fundamental concepts	9
1.2	MTJ & TMR: Magnetic Tunnel Junction & Tunneling Magnetic Resistance	10
1.3	Spin Transfer Torque effect	11
1.4	Magnetization dynamics	12
2	Simulation Part	15
2.1	Introduction	15
2.2	Sensitivity	17
2.3	Sensitivity dependence	18
2.4	Voltage dispersion	22
2.5	TMR and Voltage dispersion	26
2.6	Magnetic element	30
2.7	Switching voltage with non-uniform field	32
2.8	Vertical sensitivity	35
2.9	Lateral Sensitivity	37
2.10	Different Geometries	42
2.10.1	Two near markers	42
2.10.2	Four markers square placed	47
2.10.3	Two far markers	50
2.10.4	Two pairs of near markers placed far each other	56
2.11	Conclusion	58
3	Experimental part	61
3.1	Introduction	61
3.2	Experiment set up	62
3.3	Measurements	64
3.4	Conclusion	70
4	Conclusion	71

Chapter 1

Introduction

Over the last few years there have been done big steps with the MRAM technology. This non-volatile memory's device has incredible high endurance, low energy consumption and high thermal stability capabilities. New challenges on this topic are emerging and, in this work, we try to introduce a new use of such device. In particular, aim of this project is to simulate and characterise a magnetic field sensor able to detect possible misalignment of the order of sub micrometer range. There are some applications that need the help of sub micrometer sensor's detection, in particular very interesting are in the field of wafers alignment.

Recently, the research is going towards the 3D integration (fig. 1.1) instead of the standard planar technology for three fundamental reasons: more compactness, the device is more compact w.r.t. the planar technology and occupies less space, this helps to integrate higher number of devices at constant chip footprint; more versatility, now with the 3D integration if we want to build the device we just need to fabricate different parts and then assembly them all together, thing that was not possible with the more standard planar technology; lower complexity and lower production costs, the existing technology for the planar one is already very performing for the 3D integration.

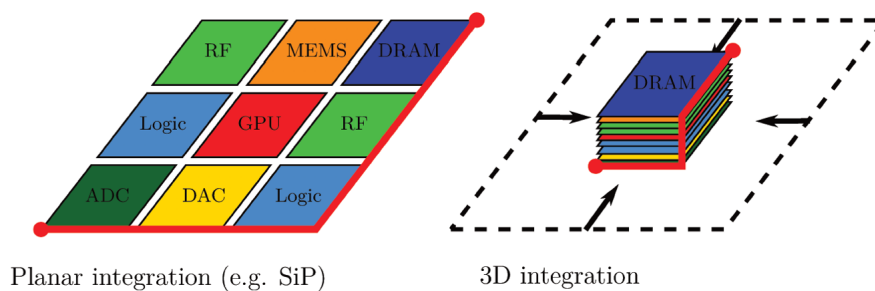


Figure 1.1: Planar integration and 3D integration structures. In 3D integration is possible to see directly from the picture the compactness and the versatility at once.

Anyway, it is important to underline the alignment issue: in order to integrate several layers one on top to the other, the wafers to be bond are subjected to misalignment between them, of the order of sub-micrometer/micrometer and this leads to a less value of current that can pass through the device, breaking down its efficiency. There are two general approaches that allow to stack different layers: the wafer-to-wafer(wtw) bonding technique and die-to-wafer(dtw) technique. The wafer to wafer bonding technique consists into bonding two wafers face to face; as it is possible to understand, at the nanometer scale, the biggest issue is to be able to align these two wafers with the highest precision possible, otherwise we could encounter diffusion of Cupper (Cu) into Silicon Dioxide (SiO_2) for instance (fig. 1.2). This technique has already high performances in terms of alignment and shows, for Hybrid Bonding($Cu - SiO_2$), a misalignment range around 200 nm [5].

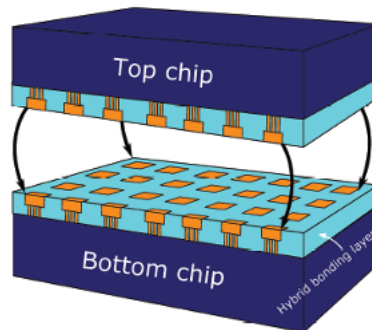


Figure 1.2: Hybrid bonding between two wafers: the two wafers are directly bonded one on the top of the other (this technique is also called direct bonding, [5]).

In die to wafer technique, instead, we need to cut one wafer into small dies and place these, piece by piece, on top to the other wafer (fig. 1.3). For what concerns this case there is a particular application that exploits the capillarity of the water in order to align the die on the wafer [3].

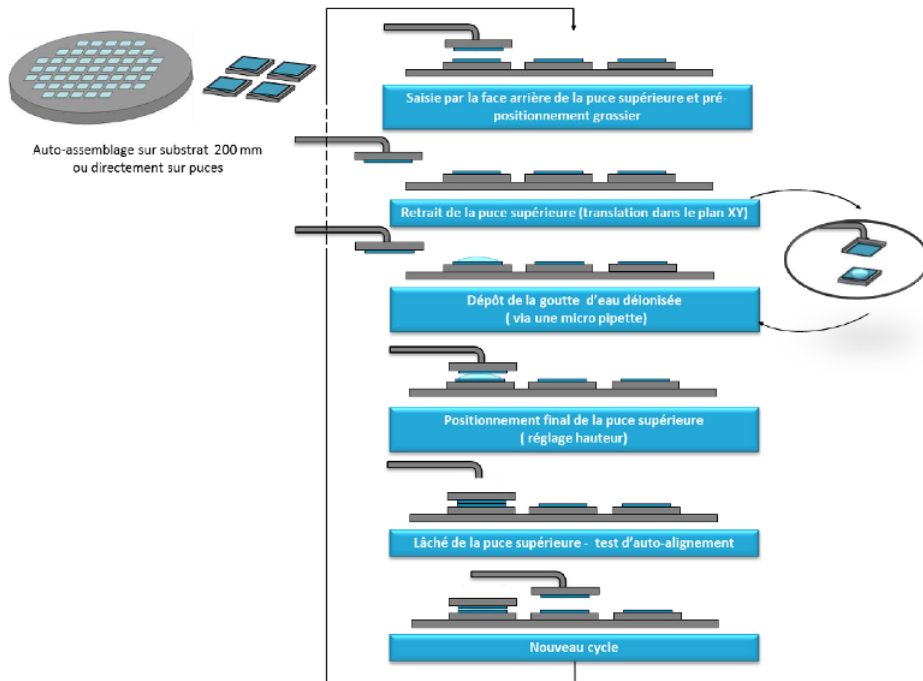


Figure 1.3: Die to wafer bonding technique: one wafer is cut and each die is placed on the wafer one by one, [3].

This second method instead, shows a larger misalignment range (around $0,5 \mu m - 2 \mu m$, [3]) owed to the high precision required to deposit the dies on the wafer's cell .

In both applications, the misalignment can be generated because of non-uniform bumps, or can be generated by removing the spacers or even due to warpage, the wafers can bend for any reasons (pressure, thermal annealing etc...), that leads to misalignment during the bonding process.

Alignment error sources:

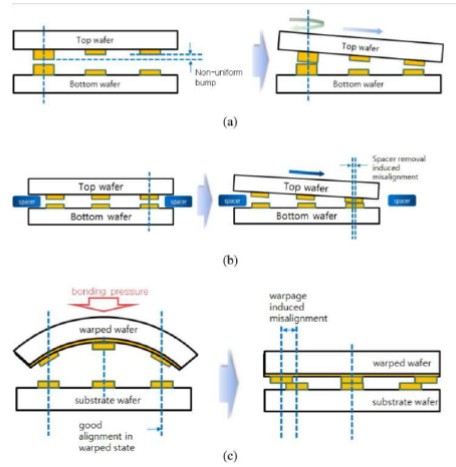


Figure 1.4: Wafer bonding: alignment error sources.

The basic idea of the project is to design a system able to detect possible misalignment both in the horizontal direction and in vertical one. To this end, the system is based on two parts: one is the magnetic element which is able to generate a magnetic field and the second part is the sensor (the STT-MRAM device), that is able to detect the magnetic field generated by the magnetic element (or easily "marker"). The sensor that we want to use is an STT-MRAM; we are able to fabricate both the magnetic element and the sensor small enough in order to integrate directly both into the two wafers.

Until now, there have been developed several magnetic sensors by using MTJ (Magnetotunnel Junction) but in this work we want to use an STT-MRAM (Spin Transfer Torque - Magnetoresistive Random Access Memory); at the moment there is not any work in literature on this topic. Nowadays, the state of the art allows to fabricate STT-MRAM up to 15 nm of diameter size of the cylindrical pillars; anyway, to our purpose, it is not necessary to challenge state of the art. In the following, after a brief introduction on the working principle of the STT-MRAM, you will find two main chapters: one dedicated to the simulation part and the other to the experimental part.

The former starts from the very beginning, by defining the most critical parameters and by identifying which are the design ones in order to get the best device's performances. Crucial will be the study of the voltage dispersion of the switching voltages that will characterise the quality of the sensor.

The latter will consist in measurements and we will discuss the agreement of the results with simulation expectations. We will characterise the device by means of a magnetic probe that will induce a magnetic field through the sensor, this will change its switching voltages for different magnetic fields applied. At the end, there is a brief conclusion that

will resume all the important steps of the project and its most important results.

1.1 Fundamental concepts

Before starting with the objective of the thesis we first described the building blocks necessary in order to understand a STT-MRAM device, in particular we will discuss the fundamental of nanomagnetism and the STT-MRAM working principles.

The easiest atom's structure consists in one electron that orbits around its nucleus (fig. 1.5). This mechanism can be seen like a current that flows into a metallic spire. As the last example, the current that flows through the spire generates a magnetic moment, so it does the same thing the electron, that, by orbiting around the nucleus, generates an orbital angular momentum \vec{S} related to a spin magnetic moment $\vec{\mu} = \frac{ge}{2m}\vec{S}$ [1] where g is the Landé factor and m the mass of the electron, for the electron $g = 2$ and $s = \frac{1}{2}$ and so a magnetic moment (or Bhor magneton) $\mu_e = \frac{e\hbar}{2m}$.

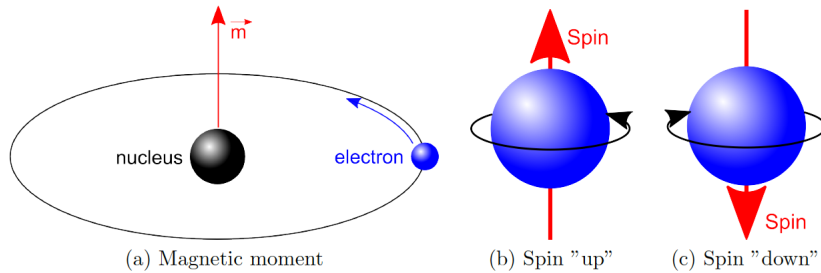


Figure 1.5: (a) Schematic representation of a magnetic field (magnetic moment) generated by the rotation of an electron around its nucleus, (b) and (c) possible spins of the electron given by the rotation on itself.

In the matter we have a total magnetic moment (or magnetization) given by the sum of the all magnetic moments of the atoms inside it. As a function of the total magnetic moment, we can distinguished different classes of materials. When an external magnetic field is applied to a material, and we see that the total magnetic moment is aligned against the direction of the applied field, we say that this material is diamagnetic, because, at the nanoscale, all the magnetic moments of the atoms have been aligned in the opposite direction of the applied magnetic field.

Instead, if the total magnetic moment is aligned towards the direction of the applied field, we call these material paramagnetic, because of the alignment of all magnetic moments in the same direction of the external field.

If the magnetization is still in the same direction of the applied field, it is also called a ferromagnetic material; the difference with the paramagnetic ones is that the former

has a magnetization order of magnitudes higher than the latter, so it has a much bigger magnetic response. This is due to the fact that the ferromagnetic materials are naturally organised into the so called Weiss domains. The Weiss domains are characterised by multiple magnetic moments all oriented in the same direction; even in that material, if it is relaxed, the total magnetic moment is still zero because each Weiss' domains is oriented towards different direction.

The things change when we remove the applied field. The paramagnetic materials and diamagnetic's ones will return with zero magnetization, while, for the ferromagnetic materials, the magnetization still remain and in order to demagnetize itself will follow the so called hysteresis loop.

The Magnetization (M , or global magnetic moment) is strictly related to the magnetic field applied B and their relation is given by the formula $B = \mu_0(M + H)$, where H is the magnetic field generated by the material (fig. 1.6), just below you can see a schematic of the so called hysteresis loop.

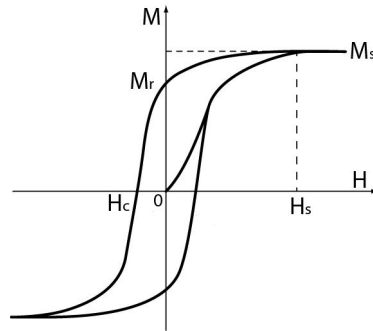


Figure 1.6: Schematic of Hysteresis loop.

1.2 MTJ & TMR: Magnetic Tunnel Junction & Tunneling Magnetic Resistance

A MTJ is a device where, the layers that compose it, are stacked in a smart way in order to obtain an artificial magnetic system able to sense an external magnetic field. The easiest structure of an MTJ is made of a thin dielectric layer sandwiched by two magnetic layers. So that, the electrons can pass through the layers by tunneling across the junction. The MRAM technology takes advantage to this effect because leads to a higher impedance w.r.t. the GMR (Giant Magneto Resistance) device, that is based on Ohmic transport. The magnetic moment of the ferromagnetic layers is aligned towards the longest axis and these can be either in parallel states or in anti-parallel states, depending on whether the MTJ is in high resistance state (Anti-parallel, fig. 1.7b) or low

resistance state (Parallel, fig. 1.7a).

In fig. 1.7, we see a schematic structure of the device, usually one of the layer is called reference layer and the other is the free layer (or storage layer). This difference is due to the fact that the former needs very high energy to change its magnetization while the latter can switch the magnetic moment even at lower energy.

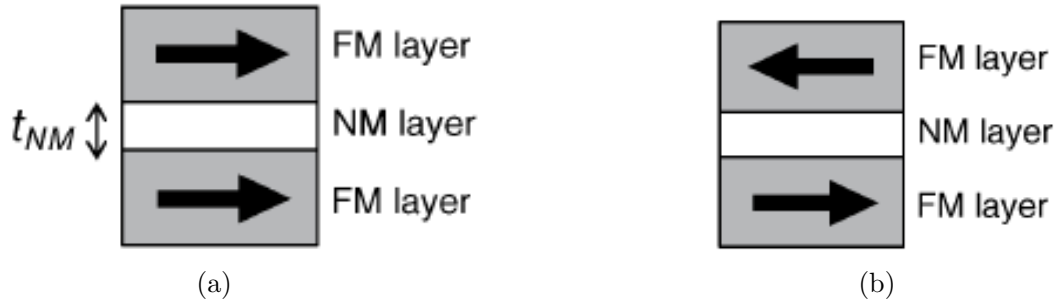


Figure 1.7: a) Parallel state, b) Anti-parallel state.

Due to the fact that the reference layer needs high energy to switch, it is easier to drive the free layer, so that, if the storage layer's magnetization is in the same direction of the magnetic moment of the reference layer we are into parallel state, if it is in the opposite direction we are into anti-parallel state.

The higher the difference between the parallel and the anti-parallel state, the better it is the device; this difference between the two states is identified by the TMR (Tunneling Magnetic Resistance) parameter. Indeed, this is defined as follow:

$$TMR = \frac{R_{AP} - R_P}{R_P}$$

Where R_P and R_{AP} is respectively the parallel and the anti-parallel resistance state. As it is possible to see the higher the difference among the resistance states and the higher is the TMR; usually this parameter is between 80% to 200%.

1.3 Spin Transfer Torque effect

In MTJ we can turn the magnetization of the free layer by means of a magnetic field, but it needs a lot of energy to produce an high enough current to generate it.

The simplest structure of STT-MRAM is similar to the one described above for the MTJ: one non-magnetic layer between two ferromagnetic layers.

In such device, the electrons pass through it perpendicularly to the junction and, when

these cross the ferromagnetic material, they are quickly spin polarized parallel to the direction of the local magnetization.

After they had crossed the ferromagnetic material and the tunnel barrier, because of the tunnel effect, they arrive in front of the other ferromagnetic material, spin polarized in the direction imposed by the previous ferromagnetic layer. If the spin polarization direction is parallel to the interface of the second ferromagnetic layer the electrons can flow; instead, if this is anti-parallel, the electrons have difficulties to pass and so they are reflected back (fig. 1.8).

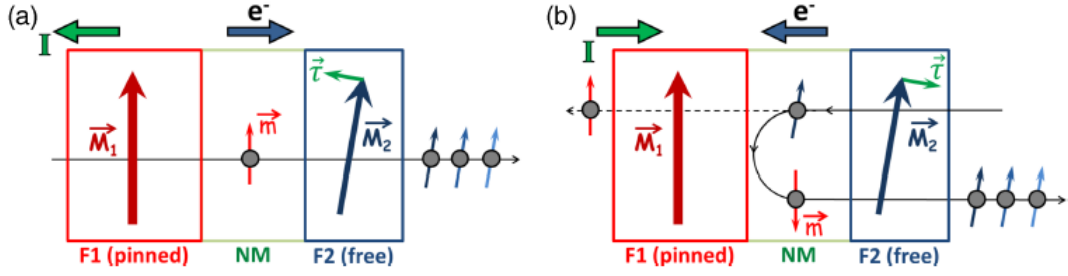


Figure 1.8: Schematic of Spin Transfer Torque: a) the spin is polarized parallel w.r.t. the local magnetization, b) the spin is polarized anti-parallel w.r.t. the local magnetization [2].

Depending whether the spin polarization is parallel or anti-parallel, the magnetization induced by the electrons to the storage layer can torque this either in parallel or in anti-parallel magnetization w.r.t. the magnetic moment of the reference layer.

We can split the induced torque into two components: one lies on the plane identified by the two magnetization vectors (in fig. 1.8 \vec{M}_1 and \vec{M}_2), and the other, orthogonal to this plane. The former is also called the in-plane torque and it is also the dominant term, while the latter is the so called out-of-plane torque.

1.4 Magnetization dynamics

We just said that the magnetization is induced by the spin-transfer-torque; but we still didn't describe the dynamic of the magnetization when is subjected to a torque. The equation that describes the dynamics of the magnetization into a solid due to a torque is the Landau-Lifshitz-Gilbert (LLG) equation:

$$\frac{d\hat{m}}{dt} = -\gamma(\hat{m} \times \vec{H}_{eff}) + \alpha\left(\hat{m} \times \frac{d\hat{m}}{dt}\right) - \gamma\hat{m} \times (\hat{m} \times a_{\parallel}\hat{p}) + \gamma\hat{m} \times a_{\perp}\hat{p} \quad (1.1)$$

The $\hat{m} = \frac{\vec{M}}{M_S}$ is the normalized vector of the magnetization (where M_S is the storage layer's volume saturation magnetization parameter); the \vec{H}_{eff} is the effective field (given by the external, anisotropy and demagnetizing field); \hat{p} is the normalized magnetization vector of the polarized layer; α is the Gilbert damping factor and γ is the gyromagnetic ratio. a_{\parallel} and a_{\perp} represent respectively the in-plane and the out-of-plane contributions; fig. 1.9 is a schematic representation of eq. (1.1).

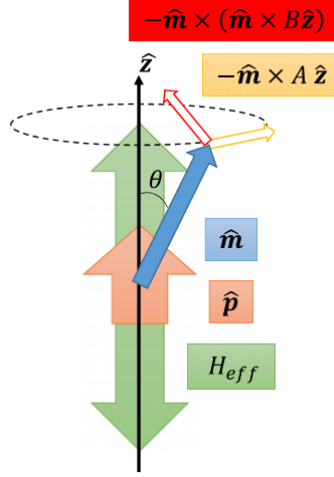


Figure 1.9: Schematic of fully perpendicular MTJ, [9].

The local magnetization of the storage layer is described by the normalized magnetization vector \hat{m} . At the equilibrium, \hat{m} is parallel to the effective field direction (\vec{H}_{eff}); once the magnetization of the free layer gains a magnetic moment due to the spin polarized current, the normalized magnetization vector (\hat{m}) starts precessing around the equilibrium position. While the vector (\hat{m}) is moving far away from the direction of \vec{H}_{eff} , the damping factor α , also known as Gilbert coefficient, pulls back the magnetization towards its equilibrium position (relaxation of the magnetization; $\alpha \sim 1 \times 10^{-5} - 0.1$, [2]).

Chapter 2

Simulation Part

In order to remind the system structure, this is characterised by two parts: one magnetic element and one is the magnetic sensor.

In the following we will simulate this two parts; we will start from the simulation of the sensor and then we will move towards the simulation of the magnetic element. At the end of the simulation we will put together the two parts in order to see how will the sensor behave if a non uniform magnetic field is applied.

2.1 Introduction

During the experiments on the STT-MRAM it has been seen that the switching voltage of this device changes with the applied magnetic field. This behavior is much clearer from an important map's device, the stability phase diagram (fig. 2.1).

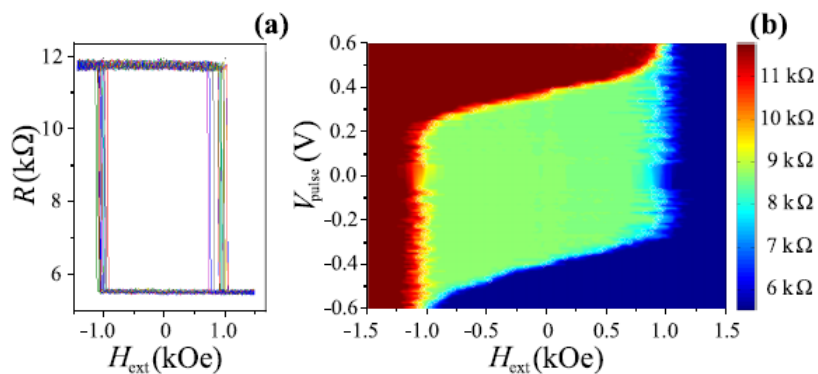


Figure 2.1: a) Hysteresis loop, b) Stability phase diagram. Experiment carried out in [9].

We address the description of this map to the next chapter where we are going to talk about the experimental results. Into this is possible to see 3 different regions: the red is

the high resistance state region, the blue is the low resistance state and the green area is the bistable region. For the moment, we only need to understand how the switching voltage changes with the applied magnetic field. The idea of the project is to use the STT-MRAM as sensor because of the linear behavior of the switching voltage as a function of the applied magnetic field (stability phase diagram, fig. 2.1). In practice, we want to be able to correlate the output switching voltage to the input magnetic field. The slope of this curve is very important since it will determine the resolution of our device, or better it affects the minimum variation of field that the sensor is able to detect. To this end, we will start with the definition of the sensitivity and find some analytic result. Then we will move forward and we start to introduce the voltage dispersion; we will see that this effect will impact noticeably the sensitivity, in particular we will see how the voltage dispersion is strictly dependent on the applied magnetic field. Moving on, we will analyse how the TMR will affect the voltage dispersion and we will discuss which is the best choice for our purpose. After that, we will introduce the voltage shift that is given by subtracting the positive switching voltage and the negative one, this is done in order to obtain a steeper behavior and so an higher sensitivity. Then, we will distinguished the vertical and the lateral sensitivity; towards the end of the chapter we'll try to use different geometries of the device and techniques in order to improve the sensitivity. The chapter will end with a small conclusion of the result obtained for the simulation part. The MRAM we are going to simulate is the one that gives us the following stability phase diagram.

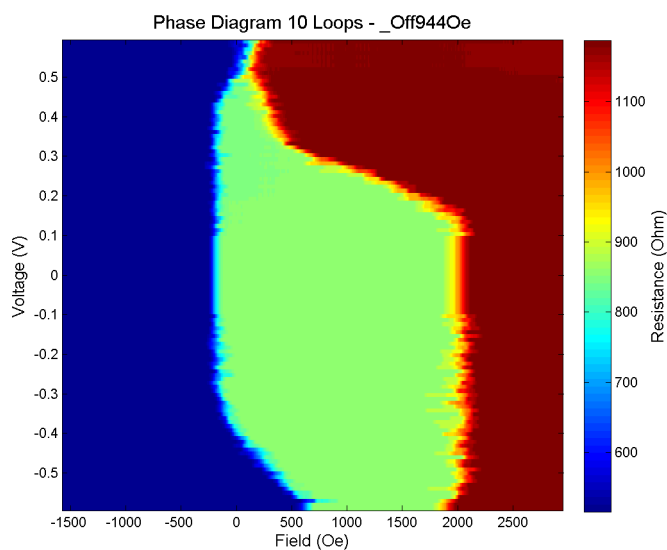


Figure 2.2: Stability phase diagram.

As you can see, the following diagram has magnetic saturation opposite to the other. You can distinguished this because the picture is mirrored like w.r.t. the previous one; indeed, the high resistance state is now on the right and the low instead is on the left.

Besides, the high resistance state has a switching voltage that is decreasing with the external field.

2.2 Sensitivity

As it is possible to see in fig. 2.2, for different magnetic fields we have different switching voltages; the heart of this project is in this linear behavior of the switching voltage. Since we are designing a sensor our aim is to make this slope steeper and so, increase the resolution of the device. From now, we will call this slope sensitivity. It is possible to analytically extract the boundaries of the phase diagram from eq. (1.1) and, as it has been done in [9], we can arrive at the current switching density expression and at the $\frac{dI_{sw}}{dH_{ext}}$ ratio:

$$I_{sw} = \frac{2e}{\hbar} \cdot \frac{t_F \alpha H_{eff} M_S}{\eta}$$

and

$$H_{eff} = H_{\perp} \left(\cos(\theta_0) \pm \frac{H_{ext}}{H_{\perp}} \right)$$

we can substitute the effective magnetic field into the switching current density formula:

$$I_{sw} = \frac{2e}{\hbar} \cdot \frac{t_F \alpha M_S H_{\perp}}{\eta} \left(\cos(\theta_0) \pm \frac{H_{ext}}{H_{\perp}} \right) \quad (2.1)$$

Equation (2.1) is the switching current density where $e = 1.602176634 \times 10^{-19} C$ is the electron's charge, $\hbar = 6.6260701510^{-27} erg \times s$ is the normalized Planck's constant, t_F is the thickness of the free layer, α is the damping coefficient, M_S is the storage layer's volume saturation magnetization parameter, H_{\perp} is the effective perpendicular anisotropy field, η is the effective spin polarization parameter and H_{ext} is the applied external field. We consider sensitivity the $\frac{dI_{sw}}{dH_{ext}}$ ratio, this ratio it has already been computed in [9] and is a measure of the variation of the switching current density w.r.t. the variation of the applied magnetic field, that ratio is equal to:

$$Sensitivity(S) = \frac{dI_{sw}}{dH_{ext}} = \frac{2e}{\hbar} \cdot \frac{t_F \alpha M_S}{\eta} \quad (2.2)$$

From eq. (2.1) we obtain the plot in fig. 2.3 and, how it is possible to see in the figure, the behavior obtained reminds the one of the stability phase diagram in fig. 2.2, there are anyway some differences due to some physics effects that we will explain in the experimental part.

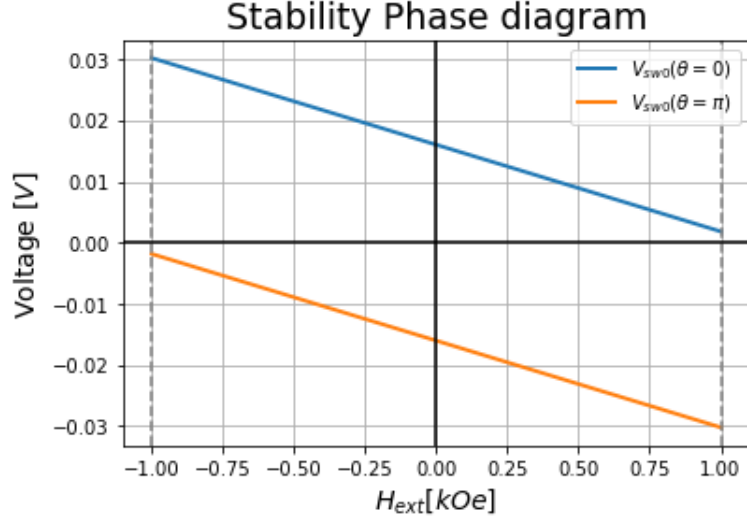


Figure 2.3: Simulation of the phase diagram boundaries.

The figure above shown is the stability phase diagram boundaries of an STT-MRAM; the device has the free layer thickness $t_F = 1.3 \text{ nm}$, the damping factor $\alpha = 0.01$, the magnetization saturation parameter is $M_S = 1030 \text{ emu/cm}_3$ and the is $TMR = 130\%$, so the effective spin polarization parameter is equal to:

$$\eta = \frac{\sqrt{TMR(TMR + 2)}}{2(TMR + 1)} \sim 0.5.$$

The resulting sensitivity it has been computed from eq. (2.2) and is $S = 8.62 \times 10^{-2} \text{ mV/Oe}$. The units of the sensitivity are in mV/Oe instead of mA/Oe because the switching current density is multiplied by the low resistance state (R_P) and by the area of the device, so we are actually considering the switching voltage instead of the switching current density; in the following we will keep this position.

2.3 Sensitivity dependence

Now that we have identified what the sensitivity actually is, we will study the dependence of the sensitivity from different parameters.

$$\text{Sensitivity} = \frac{dI_{sw}}{dH_{ext}} = \frac{2e}{\hbar} \cdot \frac{t_F \alpha M_S}{\eta}$$

In the above formula we are still not considering the writing pulse that actually affects noticeably the sensitivity of the device. So, we have to correct the above formula and introduce the writing pulse width; in [9], we can still find the expression for the sensitivity for a finite writing pulse:

$$Sensitivity = \frac{dI_{sw}}{dH_{ext}} = \frac{2e}{\hbar} \cdot \frac{t_F \alpha M_S}{\eta} \left(1 - \frac{k_B T}{\Delta E} \log \left(\frac{\tau}{\tau_0} \right) \right) \quad (2.3)$$

τ is the writing pulse width, $\tau_0 = 1 \text{ ns}$ is an attempt writing pulse width and $\Delta E = \frac{H_{\perp} M_S V_p}{2k_B T} = 53$ is the energy barrier or the so called thermal stability, where $H_{\perp} = 1129 \text{ Oe}$ and the volume is given by $V_p \sim 3.7 \times 10^3 \text{ nm}^3$ that is the volume of the domain wall. This is due to the fact that when the diameter (D) of the junction is larger than the diameter (D_n) of the domain wall, the thermal stability saturates to the value (D_n), [6].

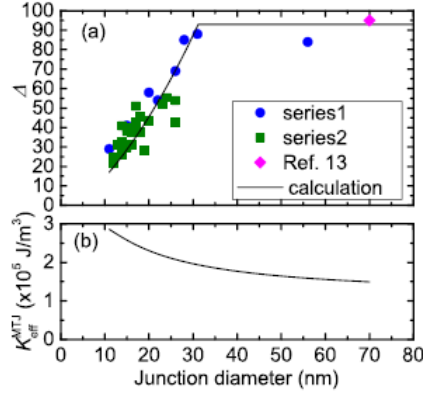


Figure 2.4: a) Behavior of the thermal stability as a function of the diameter pillar size, b) Effective perpendicular anisotropy as function of junction diameter, [6].

The sensitivity has a linear dependence w.r.t. the thickness of the STT-MRAM free layer; so, the thicker is the storage layer and the higher is the sensitivity. This is partially true, but our device works under perpendicular magnetization condition; hence, for present study, we will keep the thickness of the free layer lower than of 2 nanometers. Because of the thickness or of the diameter, the device's regime can be either in-plane or out-of plane resulting respectively in parallel or perpendicular magnetization, [4].

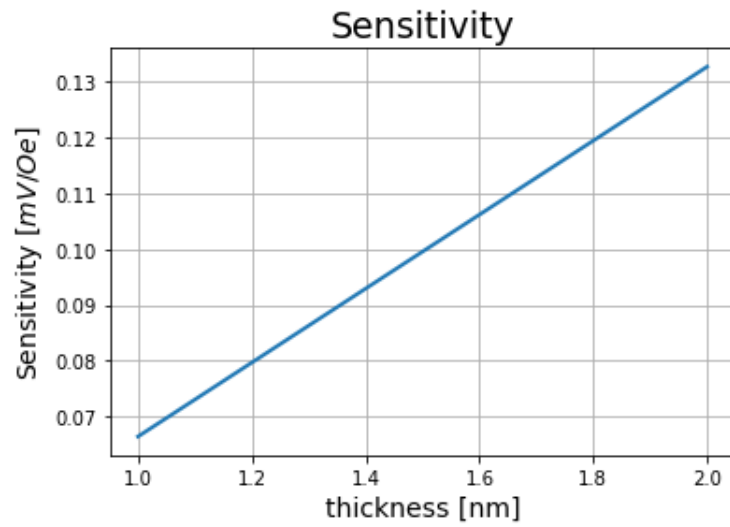


Figure 2.5: Sensitivity as a function of the thickness.

In fig. 2.5, we see that the behavior is linear and the sensitivity has doubled, indeed it passes from 0.067 mV/Oe up to 0.134 mV/Oe .

It is even interesting the behavior of the sensitivity as a function of the writing pulse width indeed, since eq. (2.3) has a logarithmic relation, the lower is the writing pulse width and the higher will be the sensitivity.

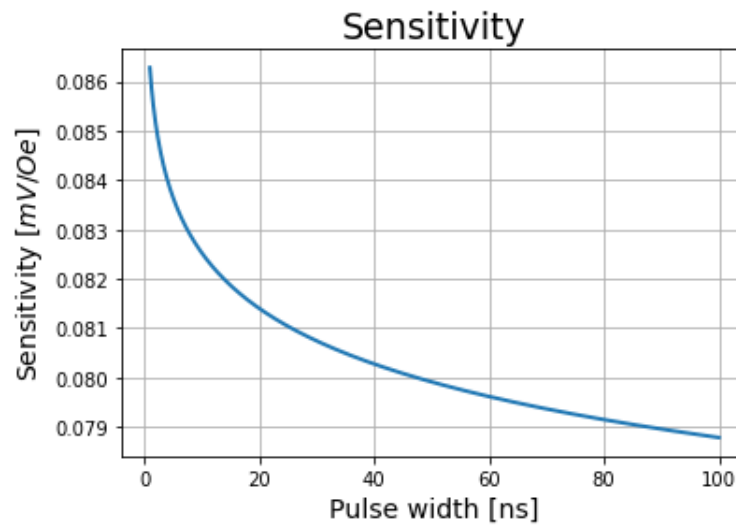


Figure 2.6: Sensitivity as a function of the writing pulse width.

We see an increase of the sensitivity of almost 9% due to the decreasing of the writing pulse width. Another parameter that has an important impact on the sensitivity is the effective spin polarized coefficient η . This parameter is at the denominator and so, the lower it is the higher will be the sensitivity. The spin polarized coefficient is anyway dependent on the TMR and so, instead of studying the sensitivity dependency from the spin polarized coefficient point of view, it is better to study how it behaves with the TMR that is more representative parameter. From eq. (2.2), it is possible to compute the sensitivity as a function of different TMR, the result is shown in the picture just below, fig. 2.7.

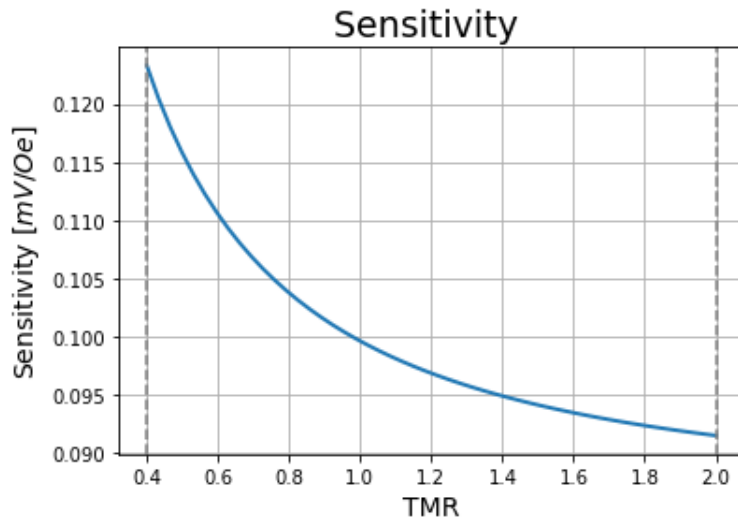


Figure 2.7: Sensitivity as a function of the TMR.

The picture shows that the sensitivity is decreasing with increasing the TMR. The TMR, as has already been explained, is a very important design parameter in the MRAM device, because it will determine the distance between the two resistance states. The two resistance states have to be well defined, otherwise it will be hard to distinguished whether we are in high resistance state or in low resistance state. The conclusion is that it cannot be possible that for a very low TMR we have a better device. In order to go deepen in this direction we will introduce a very important physical effect that affects the switching voltage: the voltage dispersion.

2.4 Voltage dispersion

When we are at constant magnetic field applied and we sweep in voltage, we will find a certain voltage for which the device has been switched from one state to the other. Now if we try to induced the same change of the resistance state for the same field applied, we sweep in voltage and we find the output switching voltage; we notice that the new switching voltage found will be slightly different from the previous attempt, this is due to the fact that there is a certain voltage range around an expected value for which the junction can switch. The switching voltage dispersion mechanism has the following dependence:

$$P(\tau) = 1 - \exp\left(-\frac{\tau}{\tau_0 \exp(\Delta)}\right) \quad (2.4)$$

This is the so called Switching Time Probability [8] where $\tau = \tau_0 \exp(\Delta)$ is the data retention time and $\tau_0 \sim 1 \text{ ns}$ is the attempt writing pulse width. Δ is the thermal stability and it has the following relation:

$$\Delta = \frac{\Delta E \left(1 - \frac{I}{I_C}\right) \left(1 \pm \frac{H}{H_k}\right)^2}{k_b T} \quad (2.5)$$

I_C is the switching current density at $\tau = \tau_0$ and I is the current crossing the device, H is the applied magnetic field and H_k is the magnetic anisotropy of the free layer. We see that the thermal stability depending quadratically on the applied magnetic field. The thermal stability is an important parameter and the higher its value the more stable is the state and the lower is the voltage dispersion.

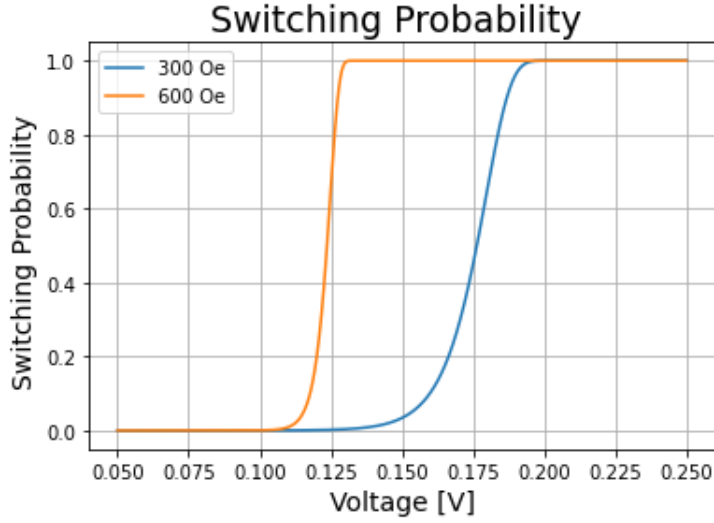


Figure 2.8: Switching probability for 600 Oe and 300 Oe applied magnetic fields.

In fig. 2.8, are plotted two different switching probabilities for 300 Oe and 600 Oe applied magnetic fields. This figure shows the behavior described in fig. 2.3, since the higher is the applied magnetic field and the lower is the switching voltage. However, the switching isn't instantaneously and there is a certain range of voltages for which both distributions have values different from 0 and 1. Another difference between these two plots is that the linear region of the curve of 600 Oe is steeper than the one of 300 Oe. This difference is highlighted in the switching current density model that is nothing more than the switching probability derivative, (fig. 2.9).

$$SCD(I) = \frac{\Delta}{I_C \tau} t_p \exp\left(-\frac{t_p}{\tau}\right) \quad (2.6)$$

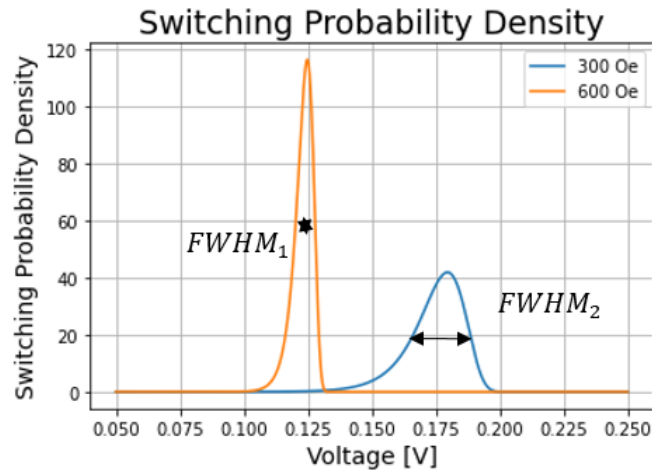


Figure 2.9: Switching probability density for 600 Oe and 300 Oe applied magnetic fields.

In fig. 2.9 is clearer that for higher magnetic fields correspond narrower voltage dispersion (FWHM) and also the expected value of the switching voltage is moving towards lower voltage values.

In fig. 2.9, the peaks are well define and it is possible to distinguished one to the other; in the picture below we see that if we make lower magnetic field steps the peaks start overlapping one with the other.

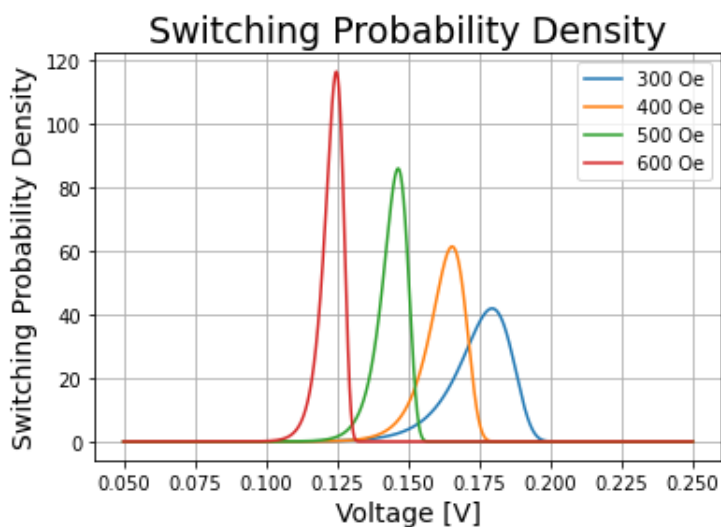


Figure 2.10: Switching probability density for 300 Oe, 400 Oe, 500 Oe and 600 Oe applied magnetic fields, the peaks start overlapping for lower magnetic field steps.

In order to understand how does it behave, we plotted the FWHM (Full Width Half Maximum) as a function of the magnetic field applied and we see that in fig. 2.11 the FWHM decreases monotonically with the applied magnetic field.

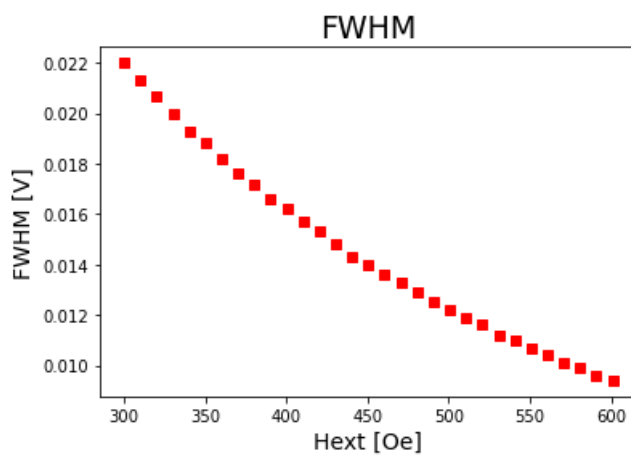


Figure 2.11: FWHM for different magnetic fields applied.

It is important now to determine the minimum field step in order to have two peaks well separated, to do so, two criteria have been used: the σ dispersion and the 2σ dispersion. The sigma dispersion requires that, in order to distinguished two near peaks we need that

the two peaks are far at least the sum of the half of their FWHM. While, if two peaks are said to be separated when the distance of the peaks is equal to the sum of their FWHM, the peaks are detected with two sigma dispersion resolution. Now we are interested to understand which is the minimum field step in order to be able to detect two different peaks.

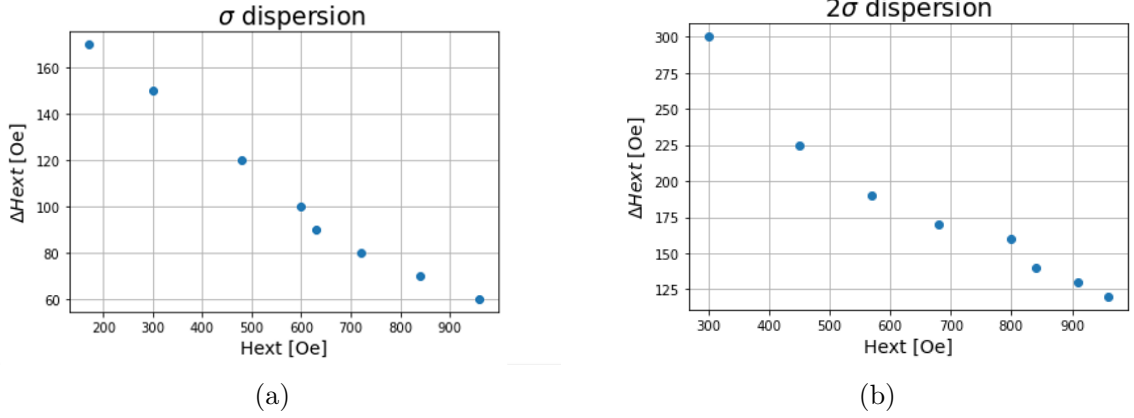


Figure 2.12: Dispersion criteria for: a) σ dispersion, b) 2σ dispersion.

In fig. 2.12 is possible to notice that the higher is the magnetic field and the lower is the field step need it in order to separate two different peaks. To compute these plots two conditions have been used, respectively for σ and 2σ dispersion.

$$\Delta V_{peaks} > \frac{FWHM_1}{2} + \frac{FWHM_2}{2}$$

$$\Delta V_{peaks} > FWHM_1 + FWHM_2$$

Where ΔV_{peaks} is the distance between two near peaks. It is important to notice that the stricter is the condition imposed and the larger would be the field step to separate two different peaks, indeed for 2σ dispersion the step field is always higher than in σ dispersion. With reference to the figure of one sigma dispersion, we see that, for instance, at 300 Oe, we need at least a step field of almost 150 Oe if we want to be able to detect two near peaks. But if the applied field is higher, the field step (suppose that the applied field is now 700 Oe for instance) necessary in order to detect two near peaks is lower (80 Oe).

2.5 TMR and Voltage dispersion

Previously we saw how, only through analytic expression, the TMR changes the sensitivity, and we saw this graph.

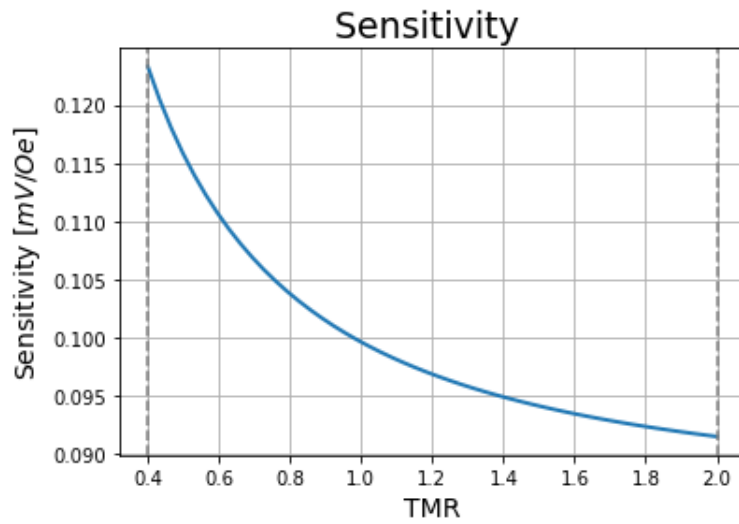


Figure 2.13: Sensitivity as a function of the TMR.

The sensitivity is increasing with decreasing the TMR, but this means that for lower TMR we have better device and this is not possible as we said before. So now, we will see why this is not possible and what is the physical effect that this important parameter induces in this device. To do so, we are interested to see how the voltage dispersion behave with the TMR. In order to understand this, we need to compute the switching probability and consequently the switching probability density.

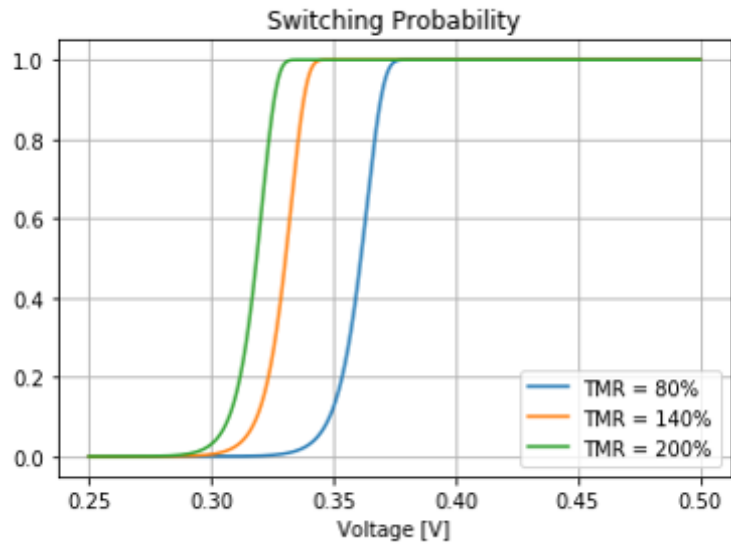


Figure 2.14: Switching probability as a function of the TMR.

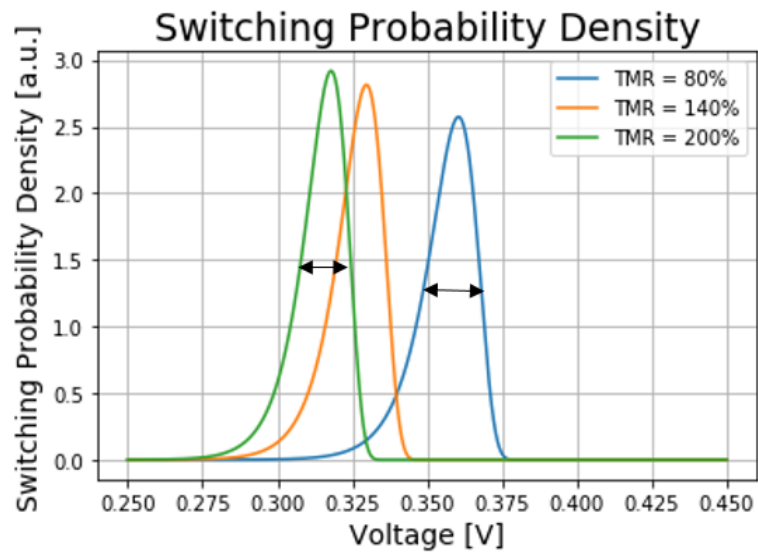


Figure 2.15: Switching probability density as a function of the TMR.

In fig. 2.14 is represented the switching probability and it shows clearly that the TMR is affecting the switching voltage and its dispersion. This behavior is much clearer in

fig. 2.15 that shows how the peak, increasing the TMR, is moving towards lower switching voltages, at the same time, it is possible to see even that the higher is the TMR and the narrower is the voltage dispersion, so this means that if we have a larger TMR, the resolution, the ability to distinguish two near peaks, increases.

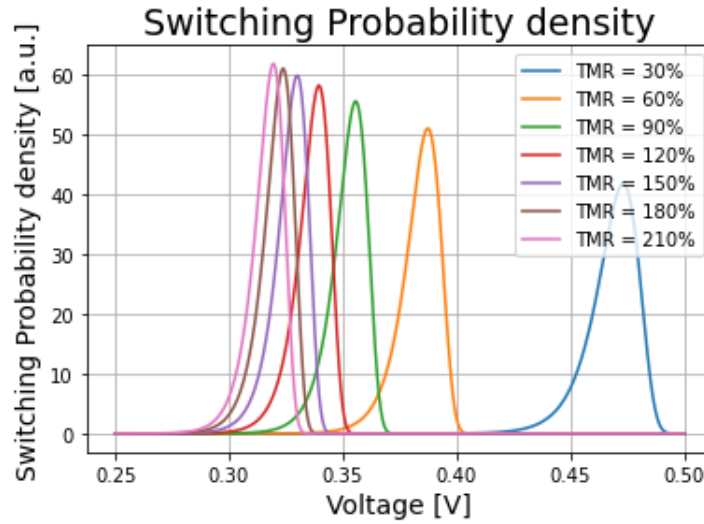


Figure 2.16: Switching probability density as a function of the TMR.

We see that increasing the TMR the voltage dispersion (FWHM) decrease monotonically (fig. 2.17). Now, how we did before, we can see how does the FWHM changes as a function of the TMR, it is straightforward that the voltage dispersion decrease monotonically by increasing the TMR.

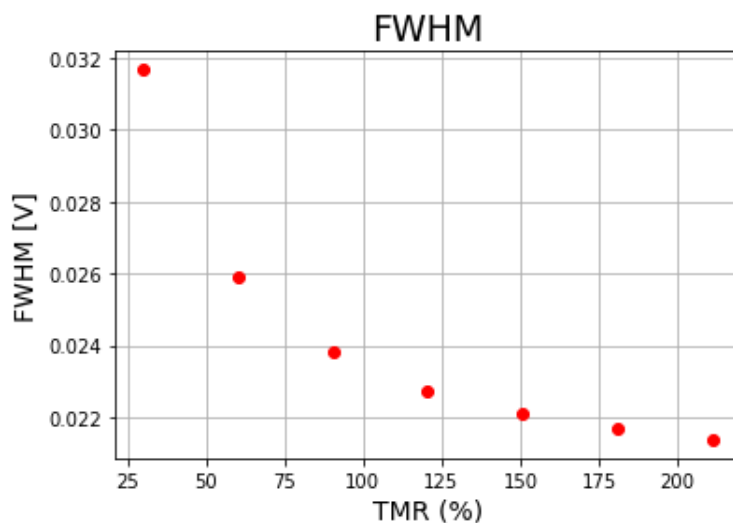


Figure 2.17: FWHM as a function of the TMR.

In fig. 2.17 is plotted the Full Width at Half Maximum for different values of TMR. The voltage dispersion computed in this figure are relative to the switching probability density of fig. 2.16. The bandwidth of the full width at half maximum converges around 0.022 V; this means that even at 210% of TMR we have a dispersion of the voltage of 22 mV. From this graph we can arrive at the conclusion that a very high TMR could be even not necessary, since from $TMR = 150\%$ to $TMR = 210\%$ we have a change lower than 1 mV.

2.6 Magnetic element

In the previous section we have seen how the sensor behaves as a function of the magnetic field applied, but until now we have only applied uniform magnetic field. In our system we have the sensor and the magnetic element (or "marker"); the latter is a ferromagnetic cylindrical pillar of sizes 100 nm height and radius of 37.5 nm. We use this sizes of the magnetic element because we need a marker that can be incorporated inside the wafer (remember that this project has as main application the wafer alignment) and because we want that the magnetic field has a good vertical and horizontal directions in order to be able to detect both horizontal and vertical misalignment.

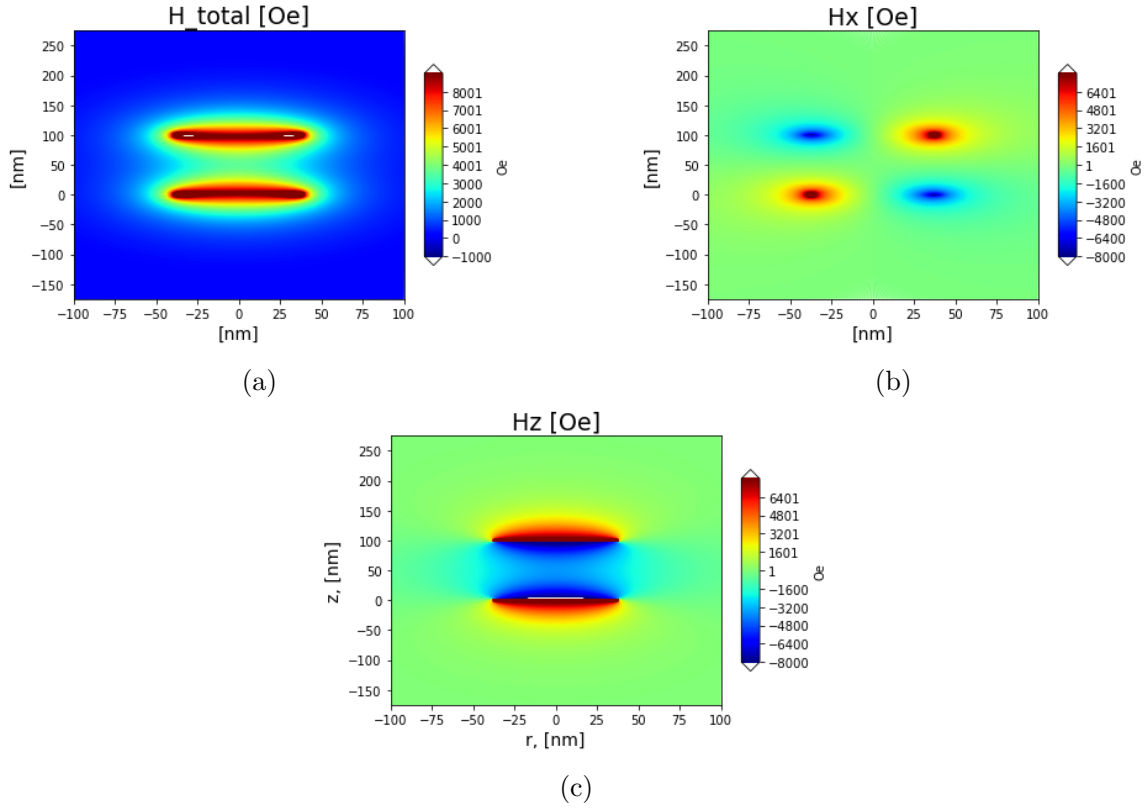


Figure 2.18: a) Total magnetic field, b) Magnetic field towards x direction, c) Magnetic field towards z direction [7].

In fig. 2.18 is shown the magnetic field behavior and its components; here we can distinguish the field in x direction (fig. 2.18b) with the one in z direction (fig. 2.18c), the sum of the two gives the total magnetic field generated by the magnetic element (see fig. 2.18a) How it is possible to see in fig. 2.18 the field generated by the marker is non-uniform and, now, its magnitude is depending on space, so, the further we measure the magnetic field and the lower will be the intensity of it. In our project we are interested in the field in the z direction due to the fact that the field is propagating perpendicularly to the plane, so we are looking at the last figure. Since the field depends on space we can study the magnetic field at different positions; to do so, we start by cutting the marker at $r = 0$ nm and the resulting field is the one in fig. 2.19.

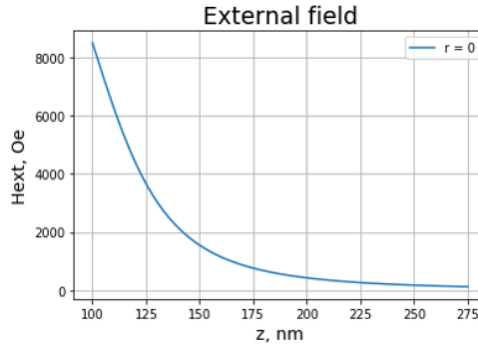


Figure 2.19: Field generated by the marker at $r = 0$.

2.7 Switching voltage with non-uniform field

As we see, the field (fig. 2.19) isn't anymore uniform and is decreasing monotonically along z direction. The field for this value of r is the highest possible, if we are going to cut the map's plot at different r , we will see that the field in magnitude will be lower; the main reason of this is due to the fact that we are not anymore centered in the marker's axis and so we are far from the source. The field in fig. 2.19 is the one we are going to use in order to compute the switching voltages. The switching voltages are given by:

$$V_{sw} = \frac{2e}{\hbar} \cdot \frac{t_F \alpha M_S V_p H_{\perp}}{\eta} \left(\cos(\theta_0) \pm \frac{H_{ext}}{H_{\perp}} \right)$$

Now if we use this field as input field for the calculation of the switching voltages we see that it takes the following shape.

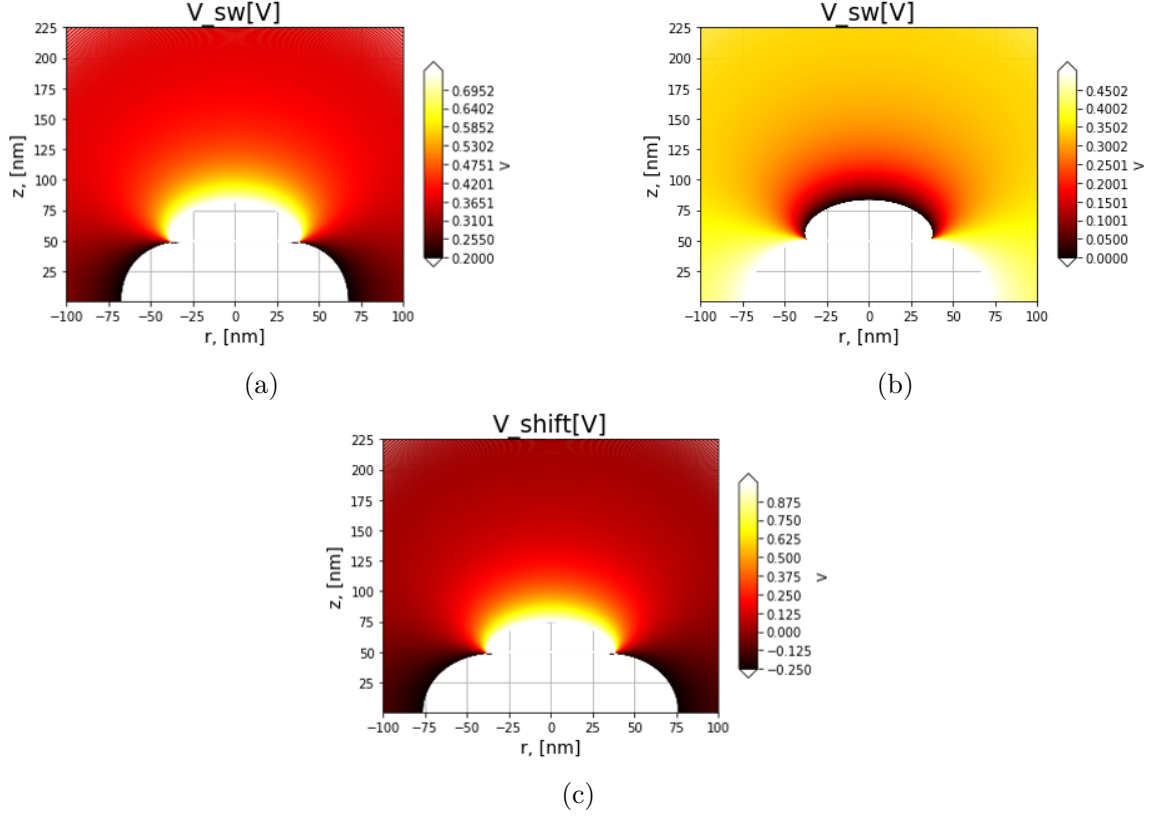


Figure 2.20: The field that have been used is the one in fig. 2.18c. a) Positive switching voltage, b) Negative switching voltage, c) Voltage shift.

The maps in fig. 2.20 are representing the switching voltages as a function of the field generated by the marker in z direction (fig. 2.18c). As described by the switching voltage formula, we can have either a positive switching voltage or a negative switching voltage, depending whether the input field is increasing or decreasing respectively. In Figure 2.20a, we see that the higher is the magnetic field and the higher is the switching voltage, this means that the field makes the switching voltage increasing. So in this case the switching process is harder (we need to apply higher voltage) in order to achieve the transition from one state to the other; in this case, we call this positive switching voltage due to the fact that the field is oriented in the direction that increase the switching voltage.

$$V_{sw}^+ = \frac{2e}{\hbar} \cdot \frac{t_F \alpha M_S V_p H_\perp}{\eta} \left(\cos(\theta_0) + \frac{H_{ext}}{H_\perp} \right)$$

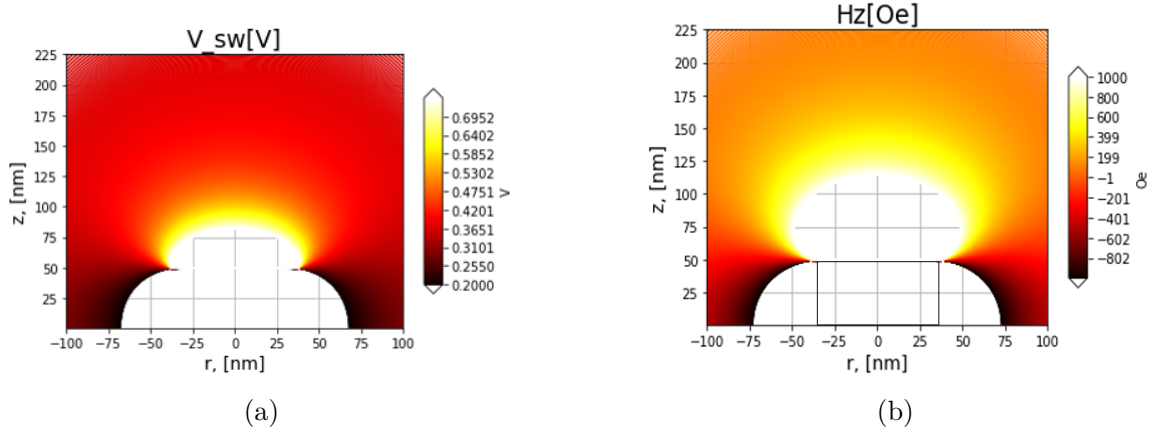


Figure 2.21: a) Positive switching voltage, b) Relative magnetic field applied.

In the figures, fig. 2.21 and fig. 2.22, are both shown the behaviors of the switching voltage and of the magnetic field, we can notice that the former follows the trend of the relative magnetic field (fig. 2.21, fig. 2.22). Viceversa, in fig. 2.22a the field makes the switching voltage decreasing, indeed, if we are far from the device (suppose $r = 0$ nm and $z = 225$ nm), the voltage necessary to switch the device's resistance state is higher. This is due to the fact that, the applied field for this value of z ($z = 225$ nm) isn't anymore strong enough to keep the switching voltage low; obviously, we call this negative switching voltage because the applied magnetic field decreases the switching voltage value.

$$V_{sw}^- = \frac{2e}{\hbar} \cdot \frac{t_F \alpha M_S V_p H_{\perp}}{\eta} \left(\cos(\theta_0) - \frac{H_{ext}}{H_{\perp}} \right)$$

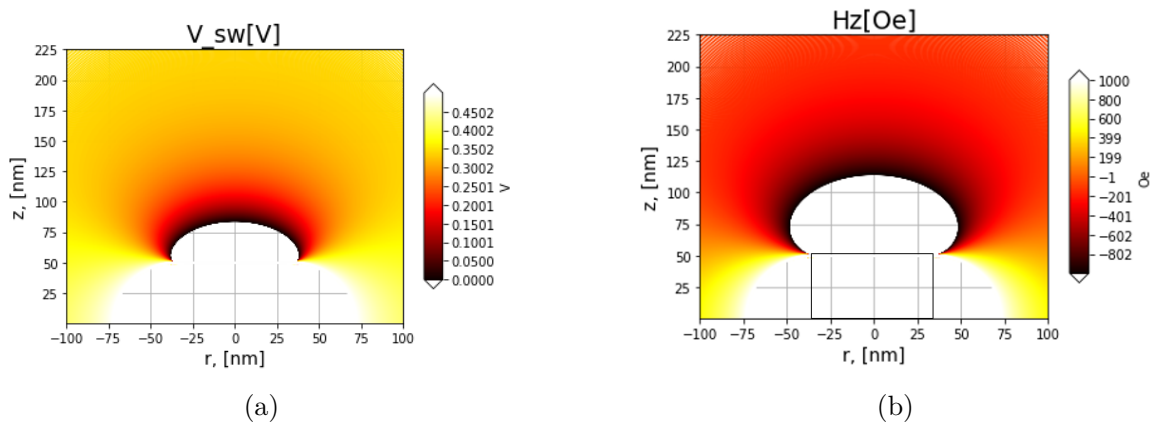


Figure 2.22: a) Positive switching voltage, b) Relative magnetic field applied.

The last of the three figures (fig. 2.20c) shows the voltage shift and is define as follow.

$$V_{shift} = V_{sw}^+ - V_{sw}^- = \frac{4e}{\hbar} \cdot \frac{t_F \alpha M_S V_p}{\eta} H_{ext}$$

Here, the voltage shift is the result of subtracting the positive with the negative switching voltage. The voltage shift is totally depending on the external field; the advantage of using the voltage shift is that in this way the slope of the sensitivity has increased of a factor 2.

2.8 Vertical sensitivity

The aim of the project is to design a system able to detect either vertical or horizontal movement of the magnetic element w.r.t. the sensor, and so, we need something that tells us exactly the position of the marker w.r.t. the sensor. In order to understand the position, we need a tool that is able to detect the vertical movement, this is done by performing the vertical sensitivity. The vertical sensitivity is a magnitude that measures the relative shift of the voltage shift w.r.t. the distance from the sensor. If we consider the voltage shift below shown and we imagine to cut the map in $r = 0$ nm, we are able to show the voltage shift as a function of the distance z (fig. 2.24).

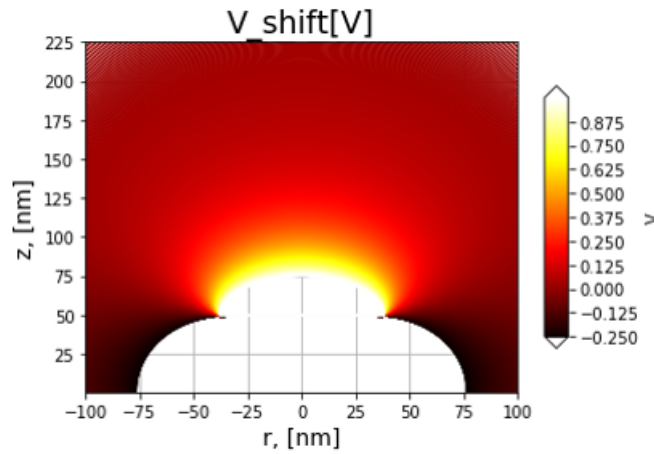


Figure 2.23: Voltage shift.

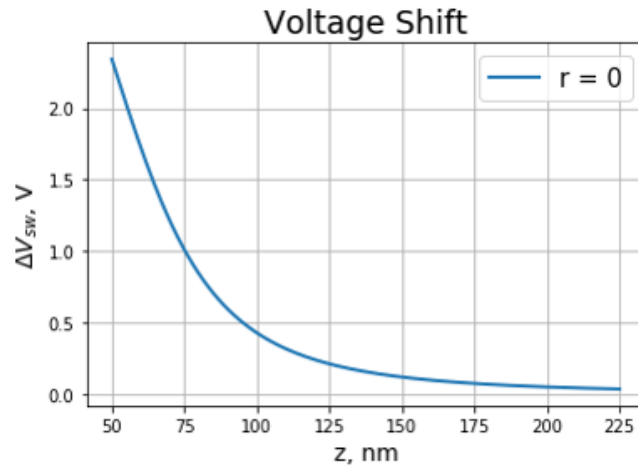
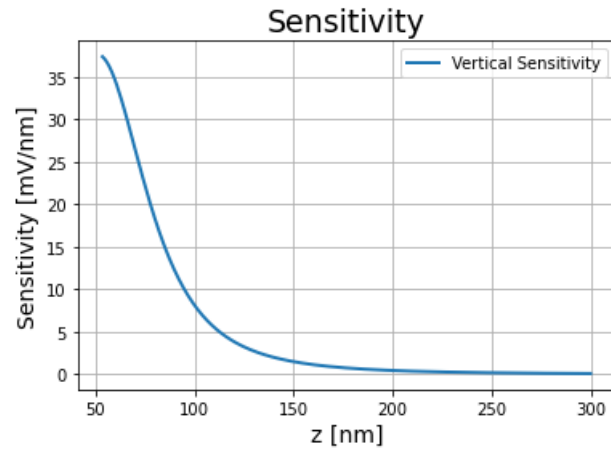


Figure 2.24: Voltage shift profile for $r = 0$ nm.

How was possible to imagine, the voltage shift is decreasing with the distance z , this is due to the fact that even the positive and negative switching voltages, far away from the source, are not affected anymore by the external field and so their difference decreases with it. The shift between the two switching voltages became irrelevant at longer distances. If we make the derivative of the voltage shift we are able to obtain the sensitivity as a function of space. In fig. 2.25 is shown the sensitivity as a function of space; how it was possible to imagine, the sensitivity at nearer distances is much higher than the sensitivity far away, this means that for lower distances from the source we are going to better detect the variation of the voltage due to a displacement along the vertical direction, this is obvious because it means that the sensor is more sensitive when is near to the magnetic element than when is far.

Figure 2.25: Vertical sensitivity for $r = 0$ nm.

2.9 Lateral Sensitivity

Now, that we have seen the vertical sensitivity we have a better understanding of the project. The sensitivity before studied is only responsible for the vertical displacement detection but isn't able to detect possible space shifts on the horizontal axis. The lateral sensitivity is the one that can detect this kind of displacement. As did it for the vertical sensitivity we have to start from the voltage shift map below shown.

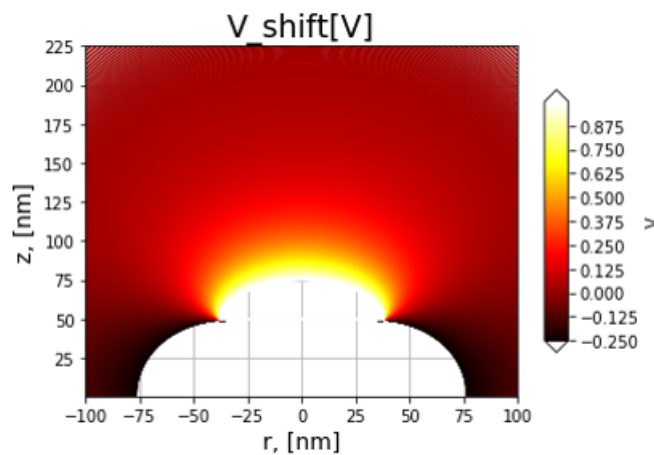


Figure 2.26: Voltage shift.

Now, considering the voltage shift we have to study the lateral sensitivity at different height and see its change. Since we have to study the voltage shift at different height we have chosen to see the behavior when the sensor is nearer the magnetic source ($z = 125$ nm) and when is far ($z = 250$ nm) in order to make a comparison. we start by studying the sensor's behavior for $z = 125$ nm, so we are considering that the STT-MRAM magnetic sensor is at 75 nm from the source (the marker end at $z = 50$ nm in fig. 2.26). At this position ($z = 125$ nm), we see in fig. 2.27 the behavior of the magnetic field.

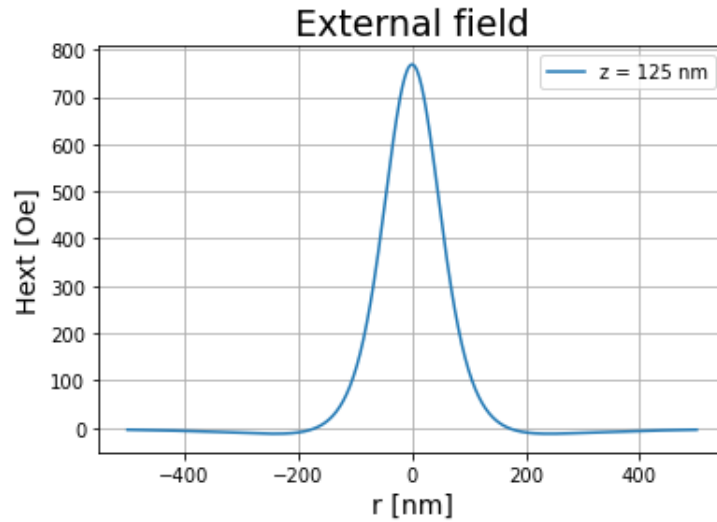
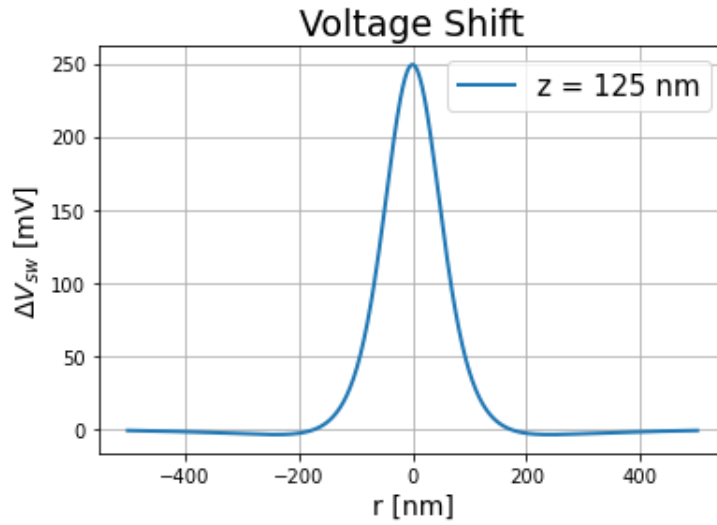
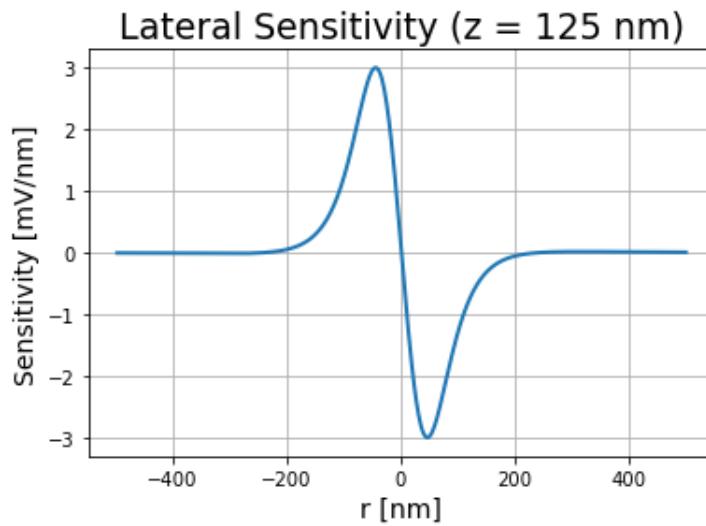


Figure 2.27: Field generated by the marker at $z = 125$ nm.

The magnetic field at fixed height is very low for large r (far from the cylindrical pillar) while we see a peak for $r = 0$ nm (where it is placed the magnet). For $z = 125$ nm and $r = 0$ nm, the field arrives to be more than 700 Oe at the center. The voltage shift given by this field is shown here below.

Figure 2.28: Voltage shift at $z = 125$ nm.

How was easy to expect the voltage shift follows the same shape of the external field; we see that in the point for which the field is maximum we achieve to have a voltage shift of 250 mV. The lateral sensitivity is given by making the derivative of such voltage shift w.r.t. the space variable r . In fig. 2.29 is possible to see its behavior.

Figure 2.29: Lateral sensitivity for $z = 125$ nm.

It is clear that the steeper is the voltage shift and the higher will be the lateral sensitivity, indeed, for $r = 0$ nm the sensitivity is null. We see that for $z = 125$ nm we are, ideally, able to detect 3 mV for each nanometer displacement, if we are in the positions that correspond to the peaks of the lateral sensitivity. Now it is interesting to see how the switching voltages behave as a function of the external field.

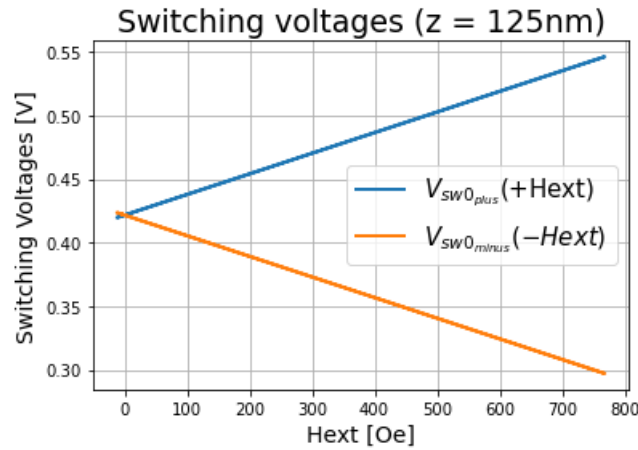


Figure 2.30: Switching voltages for $z = 125$ nm.

Here the switching voltages are functions of the magnetic field that there is for $z = 125$ nm. The voltage shift is given by subtracting the two switching voltages shown in fig. 2.30. It is clearer now that the voltage shift exploits the different behavior of the switching voltages enhancing, in this way, its slope.

If we move further away from the source, according to fig. 2.19, we should expect a lower field in the horizontal profile. This is actually what is happening; in the following figures is possible to see the differences among $z = 125$ nm and $z = 250$ nm.

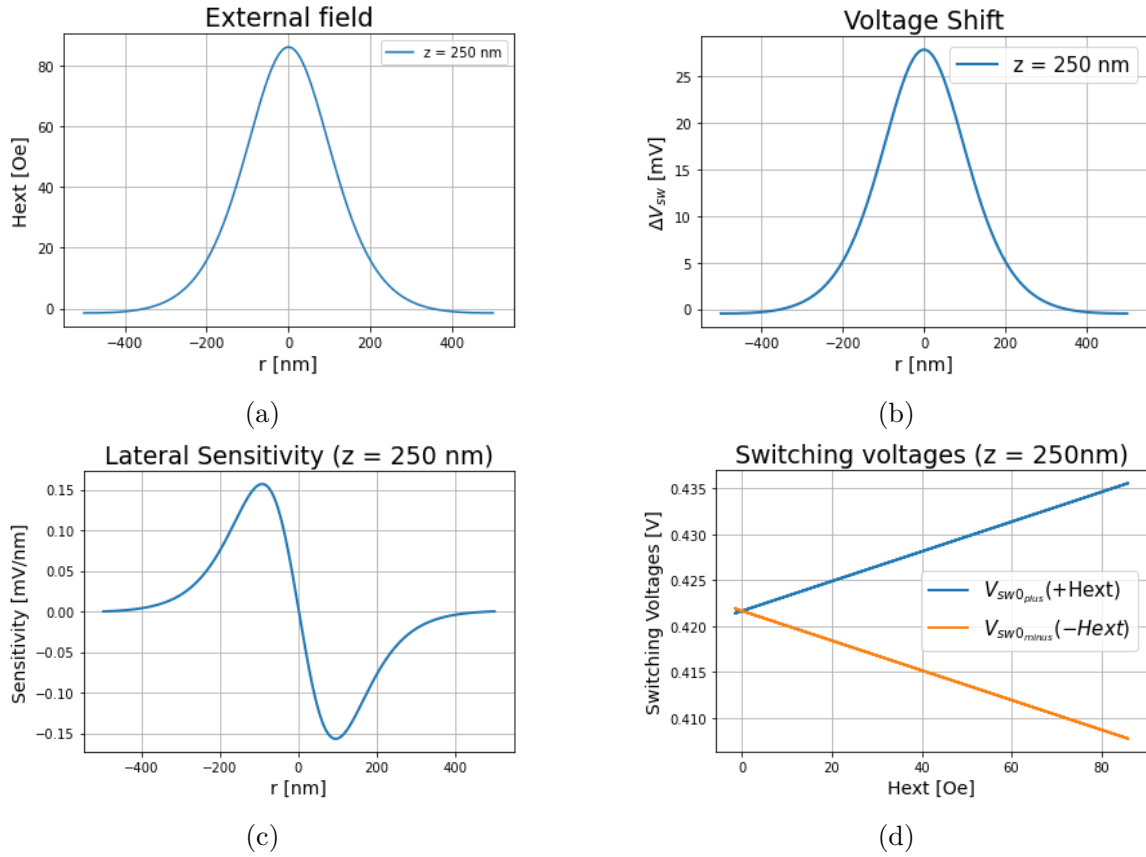


Figure 2.31: a) External field, b) Voltage shift, c) Lateral sensitivity, d) Switching voltages, $z = 250$ nm.

In these plots it is highlighted the difference of being further from the source, indeed the external field is decreased of one order of magnitude, the same has happened to the voltage shift and to the lateral sensitivity that now is able to detect 0.15 mV per nanometer. This value is quite small; in the next section we are going to see how to improve the lateral sensitivity by performing different geometries and different techniques.

2.10 Different Geometries

2.10.1 Two near markers

In the previous section we simulated one magnetic element into the wafer, but the wafer is quite large and allows us to incorporate inside it more markers in order to enhance the magnetic field and not only this.

The first attempt is to simulate two markers very near between them, like in fig. 2.32.

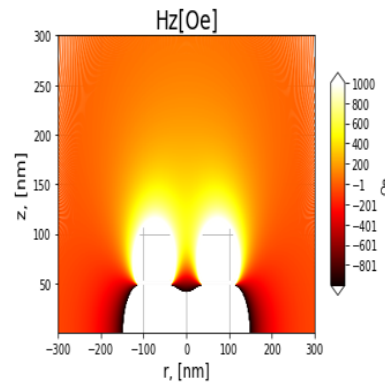


Figure 2.32: Field generated by two magnetic element at distance 70 nm one next to the other.

In the above figure the markers are placed 70 nm one next to the other, it is possible to see that the fields of the magnetic elements sum between them. It is interesting to see how the vertical and horizontal sensitivity behaves with this new configuration. The field generated is so the sum of the two fields and for $r = 0$ nm the profile is the following.

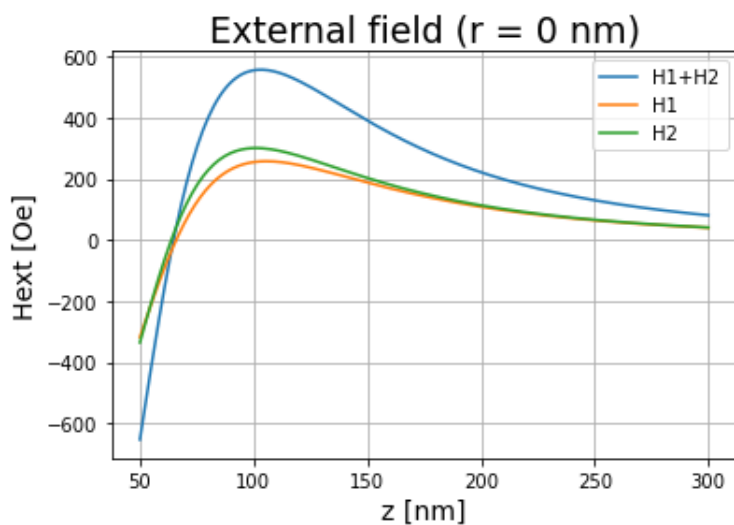


Figure 2.33: Field profile for $r = 0$ generated by two magnetic elements at distance 70 nm one next to the other.

In this particular case we are seeing the field profile for $r = 0$ nm and we can notice that very close to the sensor the field is negative and then start to be positive after few nanometers. For $z = 125$ nm, we are looking the field profile of the markers along r direction, in (fig. 2.34a) is represented the external field; this affects the switching voltage that behaves consequently fig. 2.34b

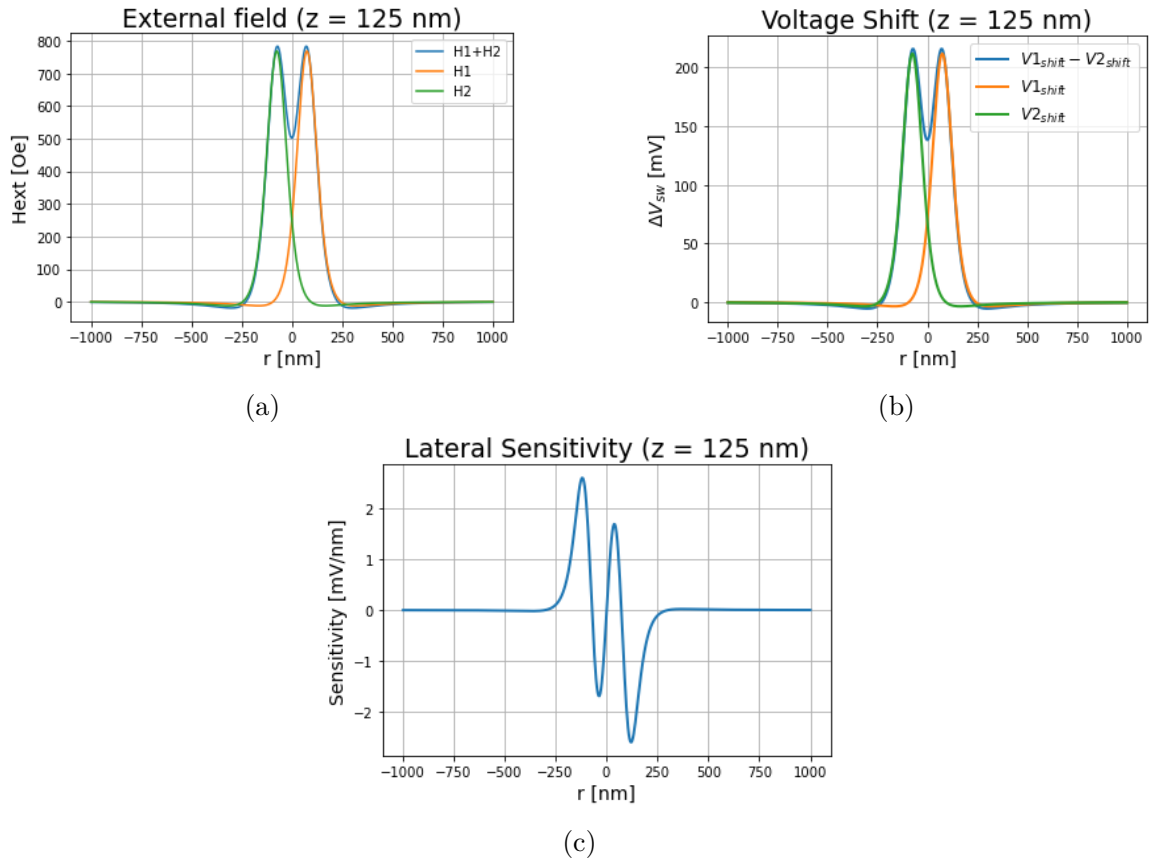


Figure 2.34: a) External field profile, b) Voltage shift profile, c) Lateral sensitivity profile. Generated by two near magnetic elements for $z = 125$ nm.

Now, since we are using more markers, the space that they occupy is larger, so the lateral resolution will gain from this; as we see the sensitivity in magnitude isn't much larger because the slope of the voltage shift is still the same.

Differently, if we measure the field at larger distances we can notice that the field is now increased, like in the case of fig. 2.35 that we are at $z = 250$ nm.

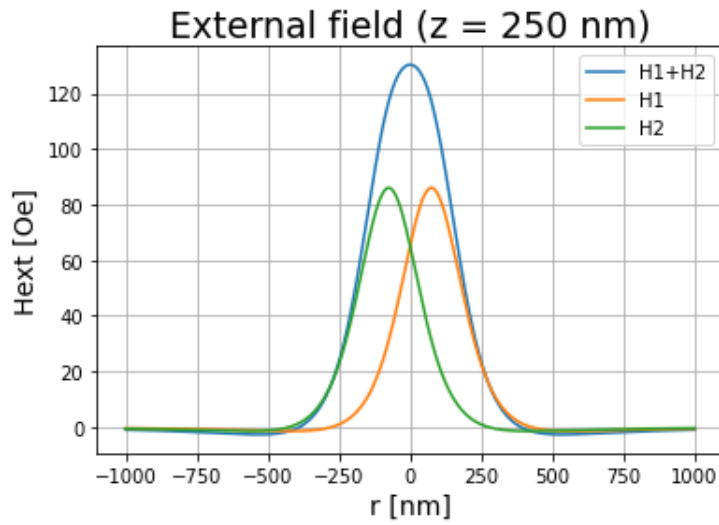


Figure 2.35: Field profile, at distance $z = 250$ nm, generated by two magnetic elements placed at 70 nm of distance.

This figure clarifies the concept of increasing the sensitivity by means of multiple markers. The green and the orange curves are the curves generated by each marker, while the blue is the one given by the sum of them. So in this way we can achieve higher vertical resolution just because we can make higher field steps at higher distances. The voltage shift has obviously the same field shape's.

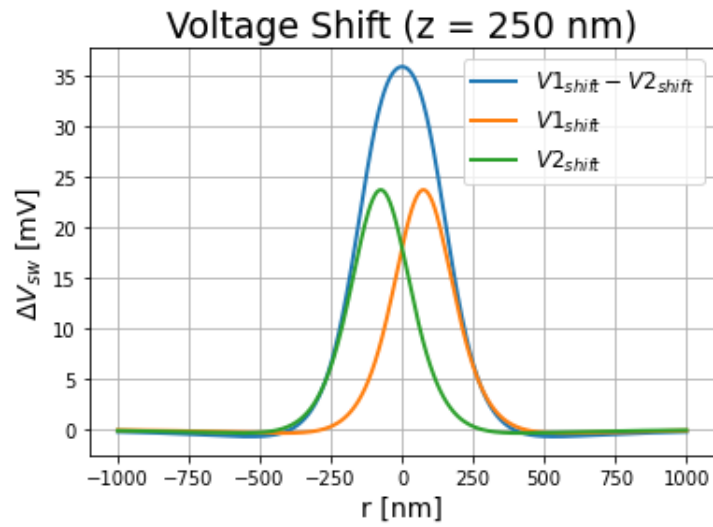


Figure 2.36: Voltage shift profile, at distance $z = 250$ nm, generated by two magnetic elements placed at 70 nm of distance.

and the relative lateral sensitivity is:

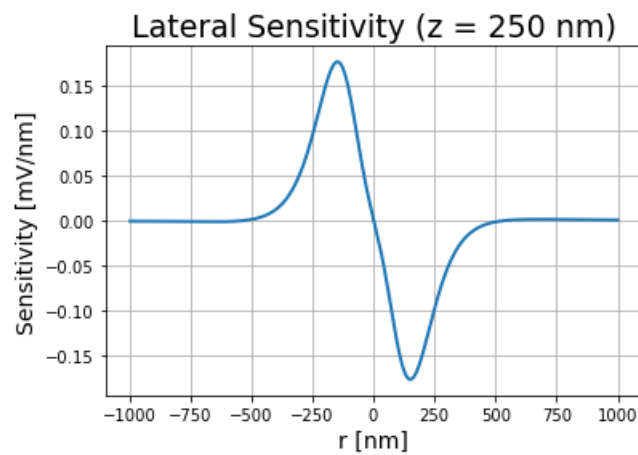


Figure 2.37: Lateral sensitivity, at distance $z = 250$ nm, generated by two magnetic elements placed at 70 nm of distance.

The lateral sensitivity is slightly increased and another interesting point is that it has greater lateral resolution since it has wider shape than the one with only one marker. For

two markers we haven't got a very high enhancement of the sensitivity, but anyway the field that we have is higher and allows us to work at further distances.

2.10.2 Four markers square placed

With two markers we saw that we are able to enhance the sensitivity of our device, it is possible to continue in this way and improve sensitivity by adding the number of markers. Here we see the differences with four markers of the same sizes square placed.

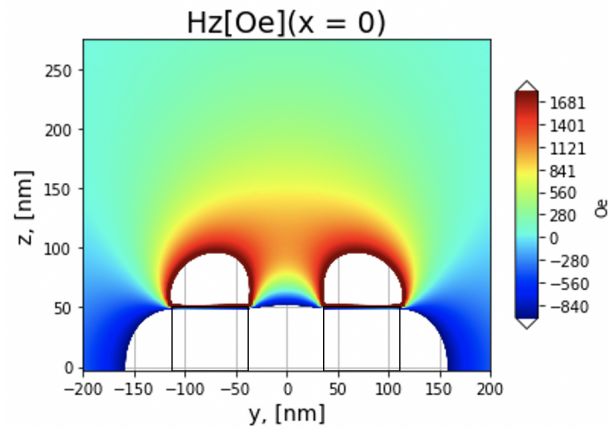


Figure 2.38: Lateral profile of the field generated by 4 markers square placed.

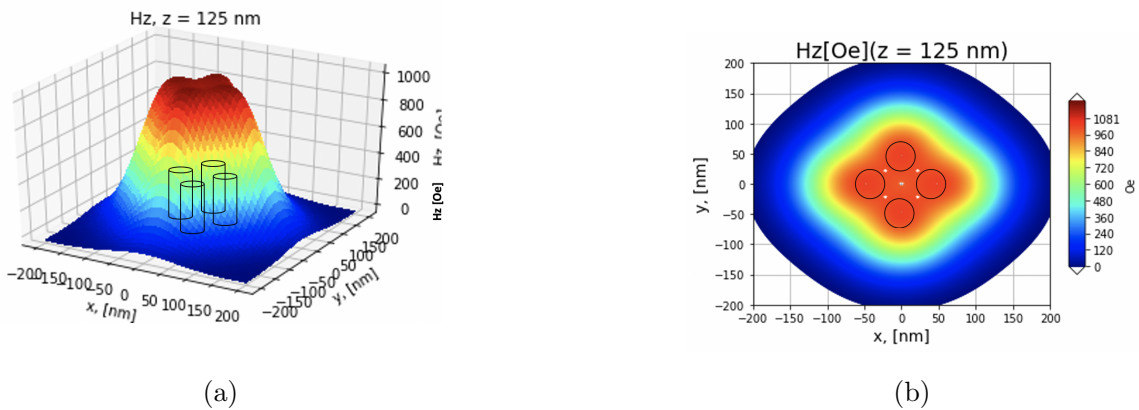


Figure 2.39: a) 3D field profile, b) Planar field profile, $z = 125$ nm.

In these figures we are showing the magnetic field at $z = 125$ nm and, how it was for the case of two markers, in the shape profile of the field it is possible to identify the four different magnetic elements, since we are near to the sources ($z = 125$ nm) and the fields aren't totally summed yet.

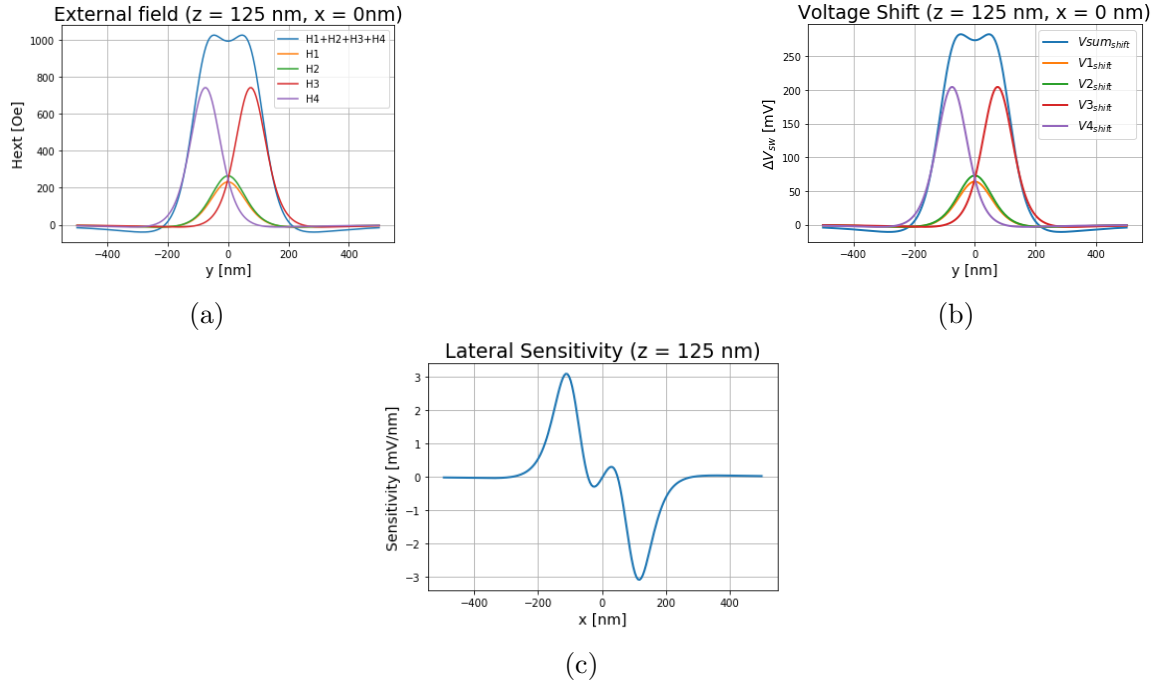


Figure 2.40: a) External field profile, b) Voltage shift profile, c) Lateral sensitivity, $z = 125$ nm

in the above figures are represented the external fields profiles, the voltage shift and the lateral sensitivity at $x = 0$ nm and $z = 125$ nm. As it is possible to see, at this height ($z = 125$ nm) these magnitudes didn't change noticeably, indeed the field is passed from 800 Oe to 1000 Oe, the voltage shift is around 300 mV and even the sensitivity is still around the same value (3 mV). But when we measure these magnitudes at further distances the things change, because we have an improvement of these.

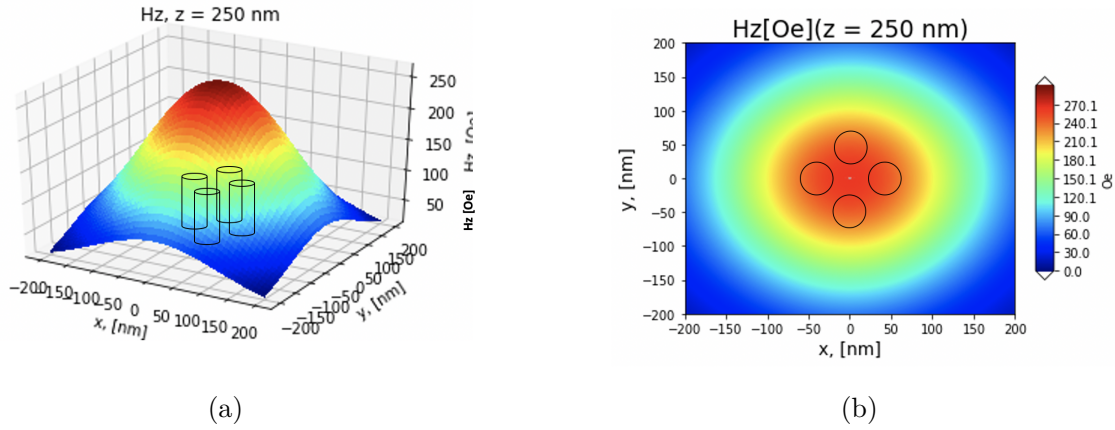


Figure 2.41: a) 3D field profile ,b) Planar field profile, $z = 250$ nm.

When we are at distances further from the device, it is not possible anymore to identify the four sources, because the 3D profile has the same shape of the field with only one marker. In this way, it is possible to obtain the same profile of one marker at further distances. The magnetic field has increased a lot from the one with one marker. In fig. 2.31a (one marker magnetic field profile), the maximum field at the same distance from the source ($z = 250$ nm) is around 80 Oe, while in fig. 2.41a we see that the maximum field arrives around 250 Oe, this means that the higher the magnetic field generated and the more sensitive we are at further distances. In the case of $z = 125$ nm this difference isn't so high because the fields didn't sum yet.

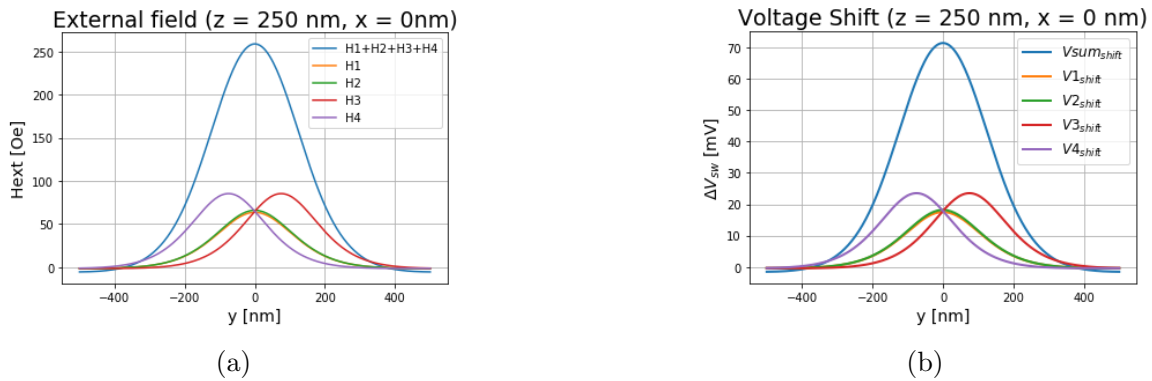


Figure 2.42: a) External field profile, b) Voltage shift profile, $z = 250$ nm and $x = 0$ nm.

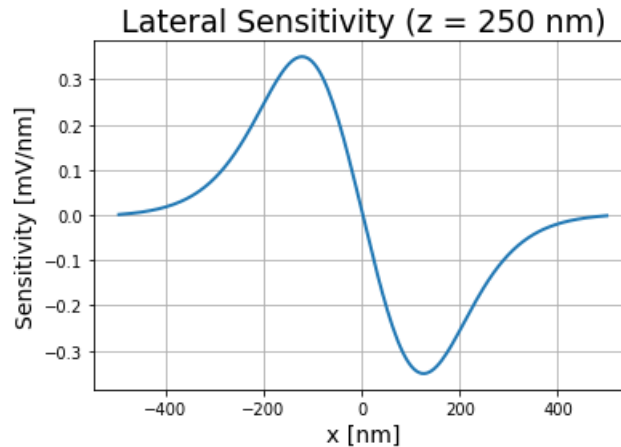


Figure 2.43: Lateral sensitivity measured at $z = 250$ nm and $x = 0$ nm for 4 markers square placed.

The lateral sensitivity has doubled its value from one and two markers and, ideally, the sensitivity is the 0.3 mV per nanometer. Even the total magnetic field and the voltage shift have been increased, the former passed from 80 Oe up to 250 Oe and the latter from 25 mV up to 70 mV.

2.10.3 Two far markers

Another possible way to increase the lateral resolution is to have two magnetic markers far between them, fig. 2.44. In this way, the peaks are separated and these will have wider lateral resolution because there is another sensitive point to the magnetic field.

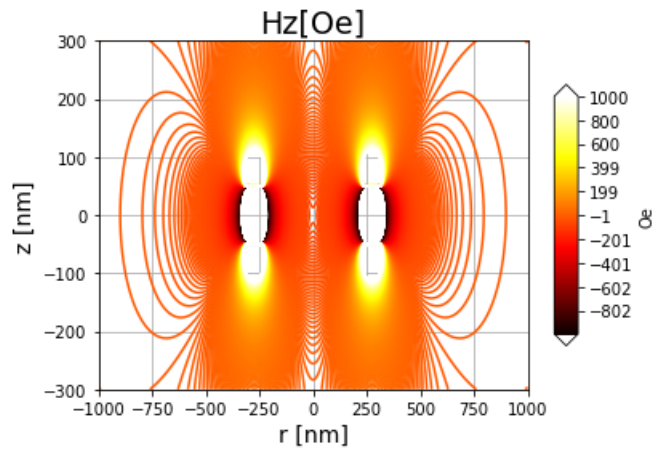


Figure 2.44: Field generated from 2 markers far between them.

How we did for the previous different geometries, we are going to show the field profile, the voltage shift profile and the lateral sensitivity. The markers are now placed at a distance of 262,5 nm. For $r = 0$ nm and $z = 125$ nm the peaks are well separated and it is possible to place the two markers even nearer and still have the peaks separated as it is possible to see in fig. 2.45.

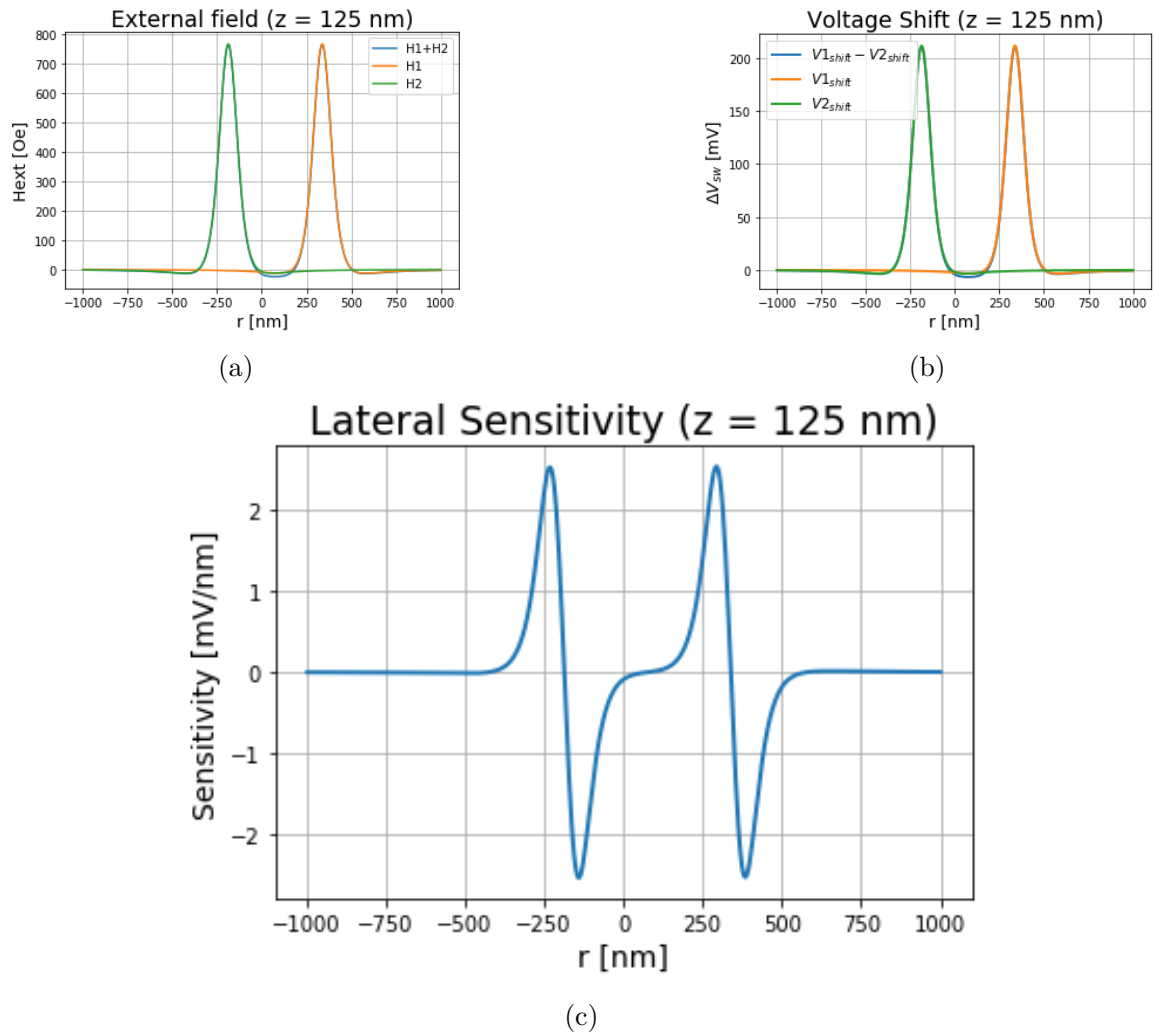


Figure 2.45: a) External field profile, b) Voltage shift profile, c) Lateral sensitivity, $z = 125$ nm.

In the lateral sensitivity we see that there is a plateau that doesn't allow to be sensitive there. In the case of larger distances instead, there isn't this issue because the peaks are already separated with the lowest resolution possible. When the peaks are wider, because we are at larger distance, the resolution is lower, in fig. 2.46 is possible to see that behavior.

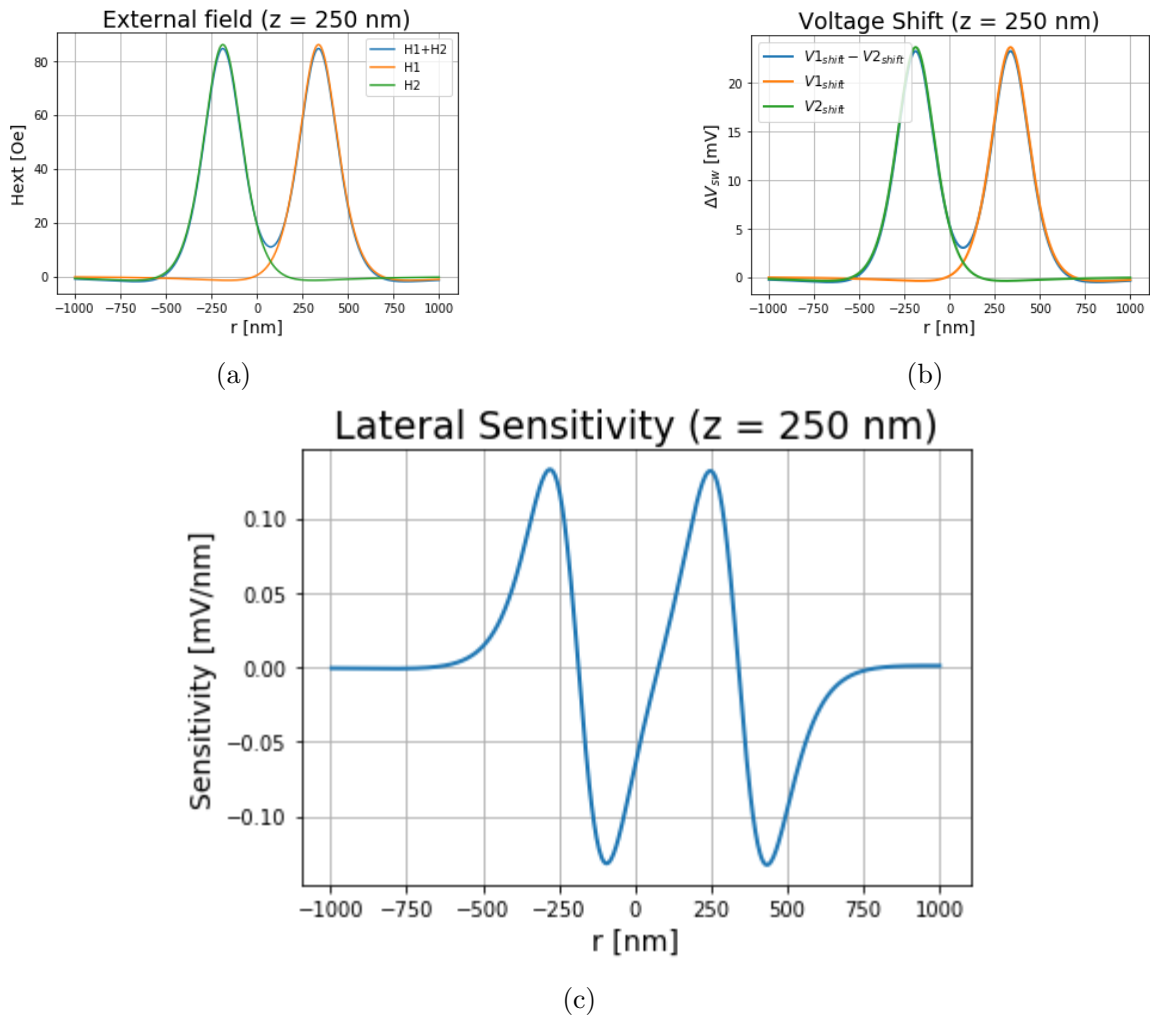


Figure 2.46: a) External field profile, b) Voltage shift profile, c) Lateral sensitivity profile, $z = 250$ nm.

In the above figures is clear that if we place the markers nearer the peaks start to overlap and we don't have anymore the behavior in fig. 2.46 but something like fig. 2.47

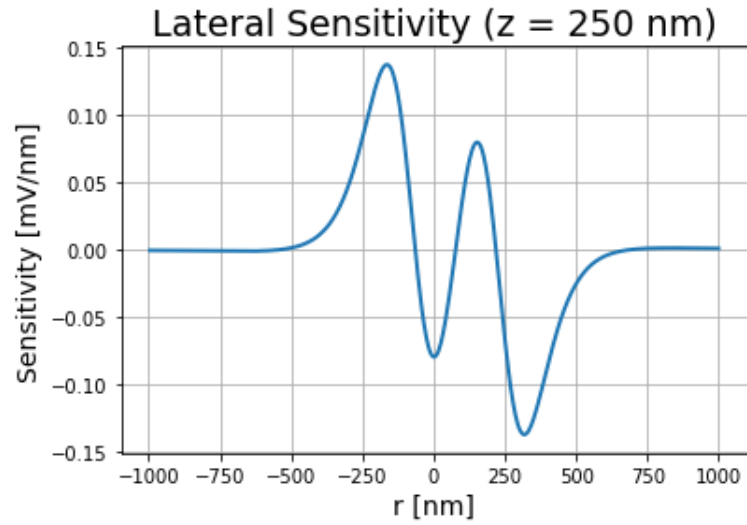


Figure 2.47: Field generated from 2 markers at distance 150 nm.

Here the distance between the markers is of 150 nm. For $z = 125$ nm we can achieve higher lateral resolution; if we place the marker nearer, we still have enough resolution in order to get a clean lateral sensitivity.

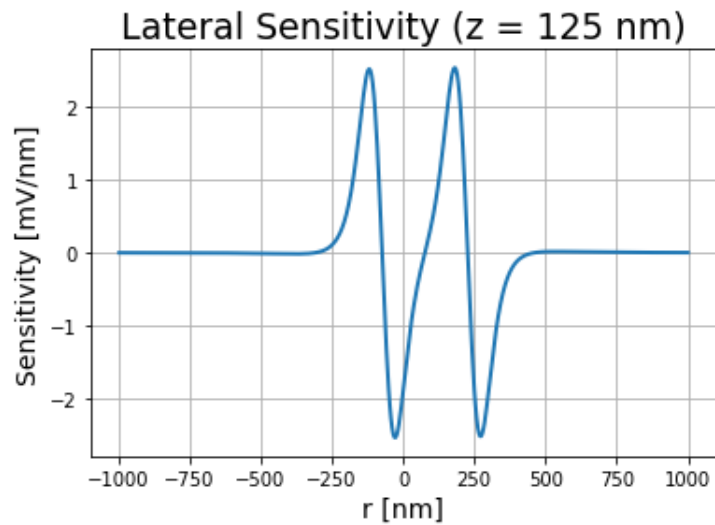


Figure 2.48: Field generated from 2 markers at distance 150 nm.

This is thanks to the fact that the peaks are still separated at this distance ($z = 125$ nm) while for $z = 250$ nm they are overlapping.

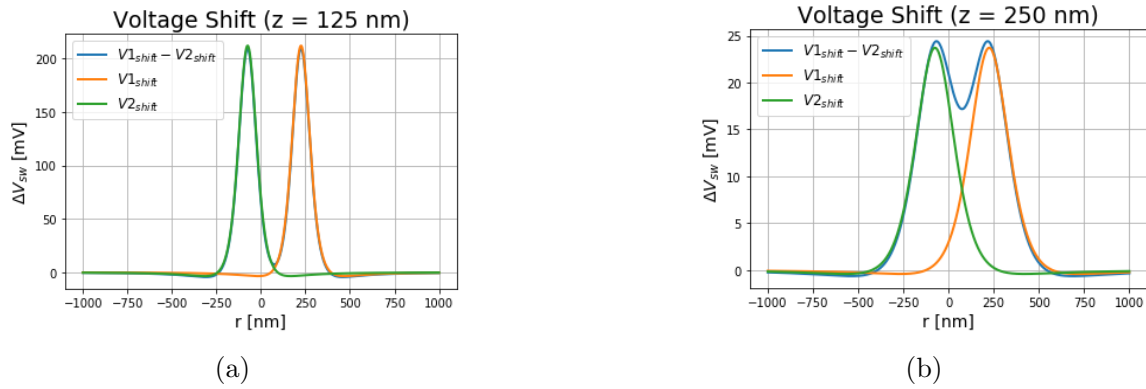


Figure 2.49: Voltage shift: a) $z = 125$ nm, b) $z = 250$ nm.

In order to give a better idea, in the following are plotted the magnitudes until here computed for different geometries for 4 markers enough far between them; the magnitudes are computed for $z = 125$ nm.

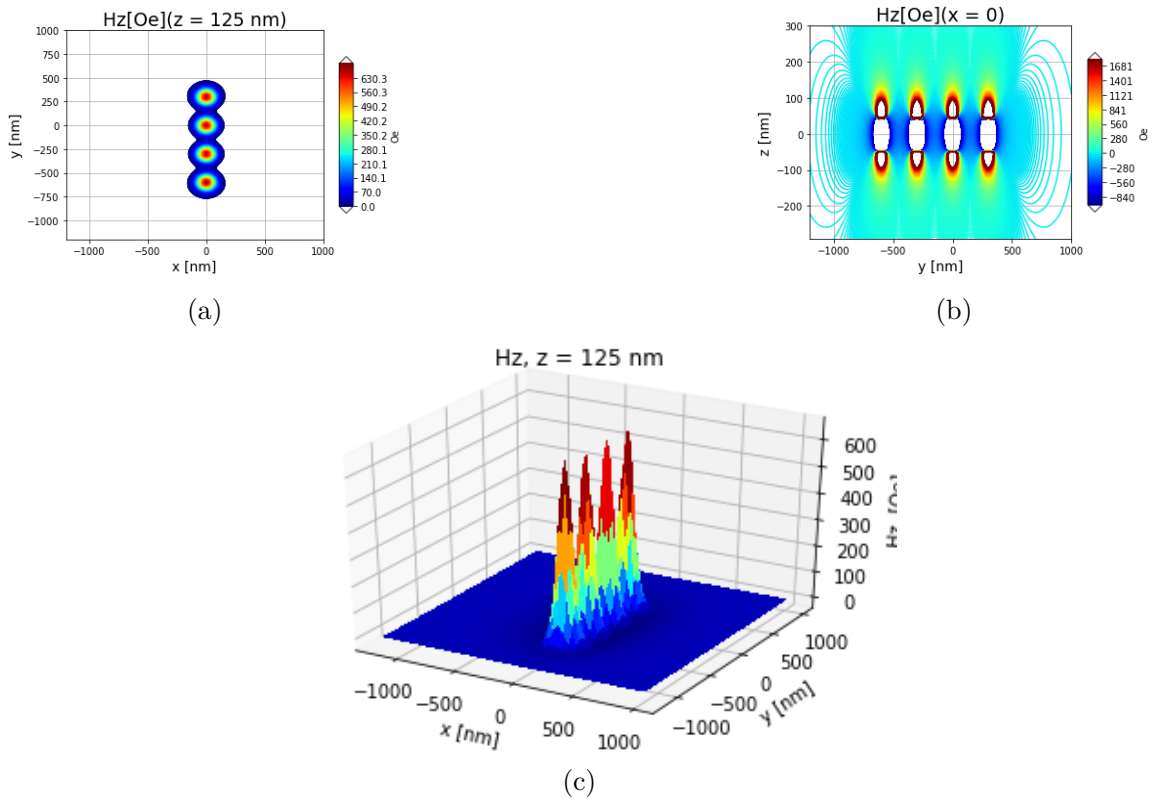


Figure 2.50: Magnetic field profile at $z = 125$ nm.

The resulting voltage shift profile and the lateral sensitivity are:

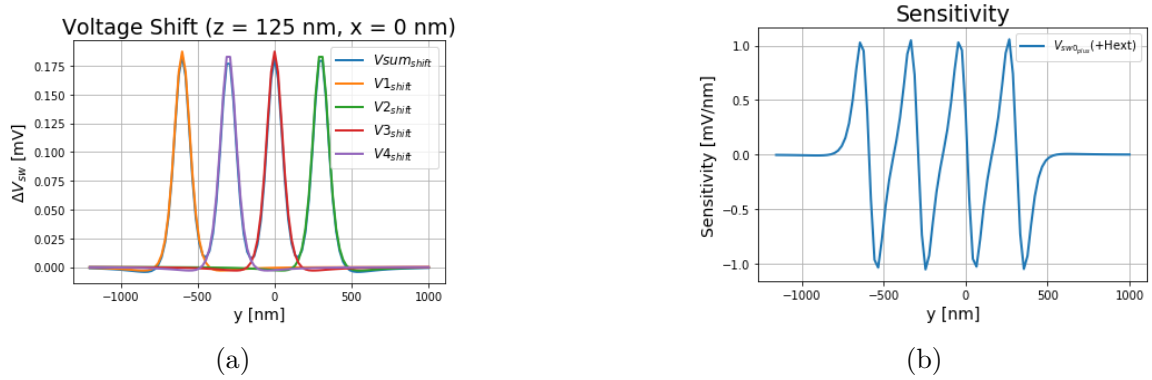


Figure 2.51: a) Voltage shift profile, b) Lateral sensitivity, $z = 125$ nm.

The peaks in the voltage shift plot (fig. 2.51a) now are very well separated and at 125 nm we are able to detect possible misalignment in horizontal direction in a range wider than $1\mu\text{m}$. The conclusion is that the lower is the distance and the better is the resolution, the issue is that we are losing resolution for further distances.

2.10.4 Two pairs of near markers placed far each other

In this section we put together the two ways to increase the sensitivity. The idea is to integrate into the wafer two near magnets placed in two far points in order that the result of the total magnetic field gives the sum only of the markers that are near, like in the figures below, fig. 2.52a.

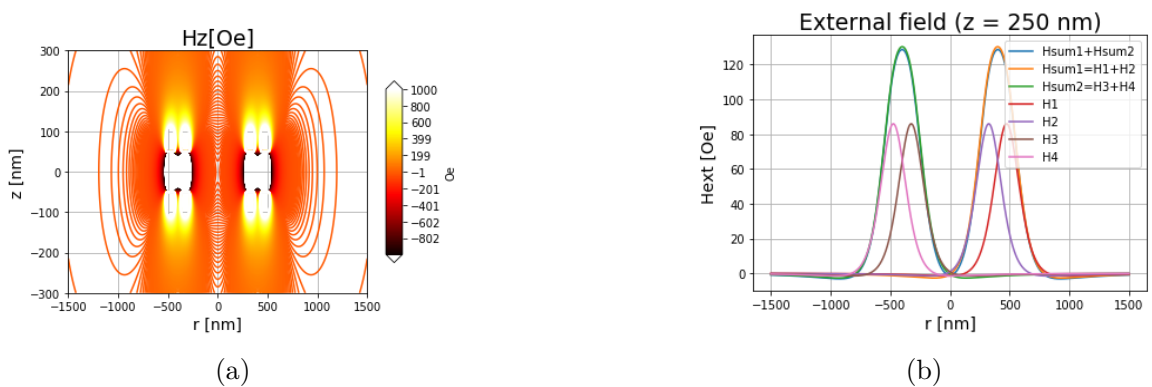


Figure 2.52: a) Magnetic field, b) Magnetic field profile at $z = 250$ nm.

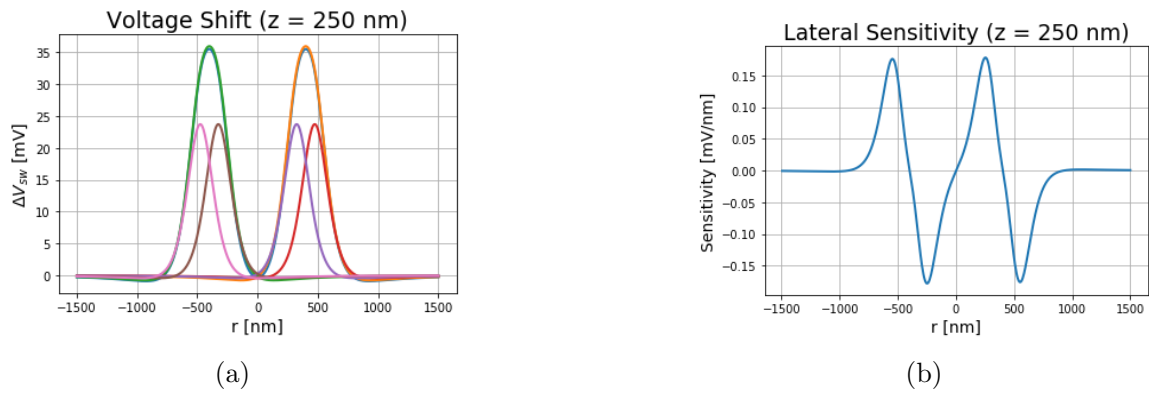


Figure 2.53: a) Voltage shift profile, b) Lateral sensitivity, $z = 250$ nm.

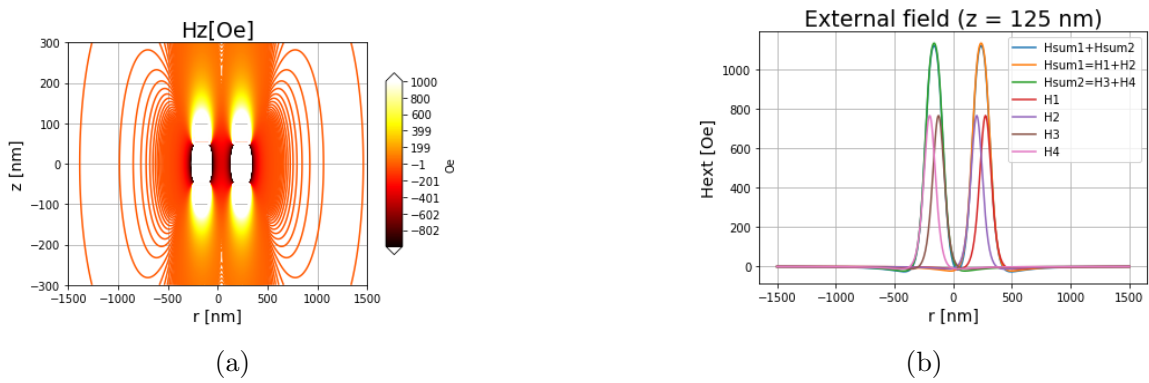


Figure 2.54: a) Magnetic field, b) Magnetic field profile at $z = 125$ nm.



Figure 2.55: a) Voltage shift profile, b) Lateral sensitivity, $z = 125$ nm.

As discussed before, the idea would be to integrate the elements in order to have higher lateral resolution by handing higher field, since is easier dealing with higher field.

2.11 Conclusion

In this chapter we have seen the simulation part of the system (magnetic element and magnetic sensor). We have seen the behavior of the critical parameters; first of all, we defined the sensitivity and we saw how the voltage dispersion affects the switching voltage and so the resolution of our device. We ended that the higher is the external magnetic field applied and the lower is the voltage dispersion; thanks to this, we arose to the fact that, the lower is the voltage dispersion (FWHM) and the smaller is the detectable step of the applied magnetic field, given a certain switching voltage as output. Then we moved forward and we discussed the issue of the effect of the TMR parameter and how the voltage dispersion plays a fundamental role in this parameter. Indeed, only by means of the analytic expression, the conclusion was that the lower is the TMR and the better is the sensitivity of the device; but, it isn't possible that for lower TMR we have a better device, and so, we have investigated the link among the voltage dispersion and the TMR. We have seen that, the higher is the TMR and the lower is the voltage dispersion; so, increasing the TMR, we have a better resolution of the detectable step of the magnetic field.

Until this point, we have simulated all the magnitudes with a uniform magnetic field applied, but, the field that actually will be in input of the sensor is non-uniform. With a non-uniform magnetic field we extracted the switching voltages and we defined the voltage shift in order to increase the resolution of the device. Then, we defined the vertical and the lateral sensitivity, that are responsible of the detection of the vertical and horizontal displacement respectively. We saw the possible ways to enhance the lateral sensitivity and we have seen two possible methods, in one case we can use more markers near in order to have a larger field making them the sum; in the other case, we placed

more magnetic markers, by don't letting them overlap, in order to have a larger surface sensitive to the horizontal displacement. Anyway, what is possible to do next is to create different geometries, maybe with different markers sizes in order to make the peaks of the switching voltage steeper and so the lateral sensitivity larger.

Chapter 3

Experimental part

3.1 Introduction

The STT-MRAM is a device that is able to have two different resistance states, it is possible to switch from one state to the other by providing a voltage pulse or by applying an external magnetic field. The state can switch even by providing both magnetic field and voltage pulse, but, in this case, for different magnetic fields applied, the voltage pulse required, in order to enable the switch from one state to the other, will change accordingly to the stability phase diagram (fig. 3.1).

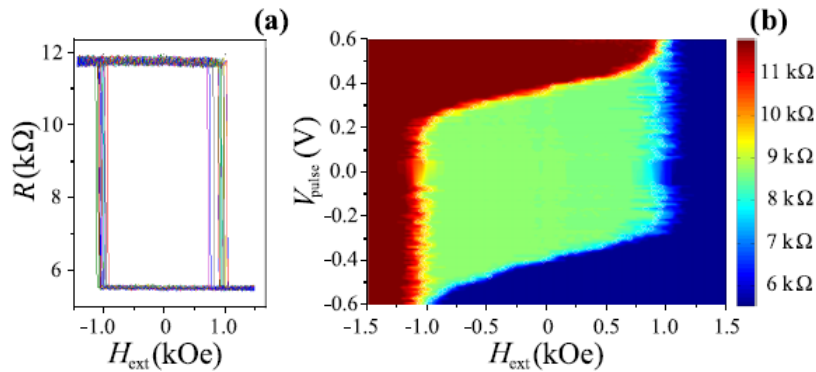


Figure 3.1: Experiment carried out in [9].

The experimental part, of the STT-MRAM as magnetic sensor, is possible to do it in two ways: the first one is to fix the magnetic field and sweeping in voltage by changing the voltage pulse amplitude and see when it switches and then repeating this for different applied magnetic fields; the second one is to keep fixed the voltage pulse and then sweeping in magnetic field in order to build in this way the so called stability phase diagram

(fig. 3.1). In fig. 3.1, the stability phase diagram is the map with the three different colors; the red color is the high resistance state, the blue is the low resistance state and the green is representing the bistable region. This map is very useful because from it, it is possible to see how the switching voltages change as a function of the magnetic field; this change is linear and it is very interesting in order to make a magnetic sensor, the steeper is the behavior and the higher is the resolution of the sensor.

3.2 Experiment set up

The experiment set up is a system of different tools. So, in order to understand each part of the set up, we have to focus on what we are looking for; we are interesting in characterizing magnetically and electrically a device called STT-MRAM. When we want to characterize electrically something, it means that we have to let pass a current through the device. To do so, we need two electrical contacts in order to apply a voltage difference; fig. 3.2 is a picture taken from the laboratory and shows the prober that is set in order to access the STT-MRAM contacts. The prober is the black rod with two tips at the end of it, the tips are responsible of the voltage difference applied to the contacts, once they are lying on them.

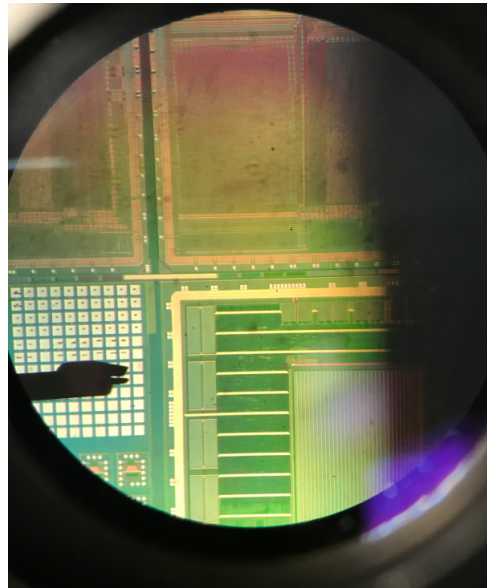


Figure 3.2: Image of the wafer used.

In fig. 3.2, the MRAM are the cells array on the left of the figure, the contacts of these are the square region linked by a small junction between them, these small junctions are the Magnetic Tunnel Junctions (MTJ). In fig. 3.3 is possible to see that some contacts have the MTJ while others don't. If we are going to characterize two different contacts

without the MTJ, we will notice it thanks to the fact that the resistance would be very high since there isn't any the junction.

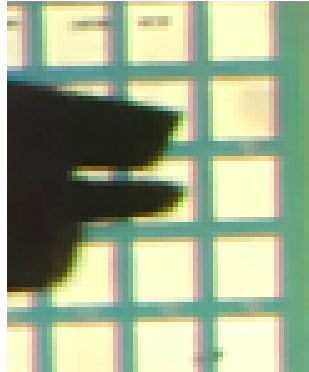


Figure 3.3: MRAM contacts.

In order to see where exactly placing the prober, an optical microscope is used. The part just described is for applying a voltage difference; then, in fig. 3.4 is possible to see the magnetic tip that generates the magnetic field that we will use to allow the switch of the junction. The magnetic field is provided by letting pass the current through the metallic red coil that induces the magnetic field, since is wrapped in circular way like in fig. 3.4. The magnetic field generated has 3 millimeter of horizontal uniformity. Below the tip, it isn't possible to see very well, but there is the prober with which we apply the voltage difference. Below the prober there is the wafer placed on a plate that is possible to move on the x,y and z axis.

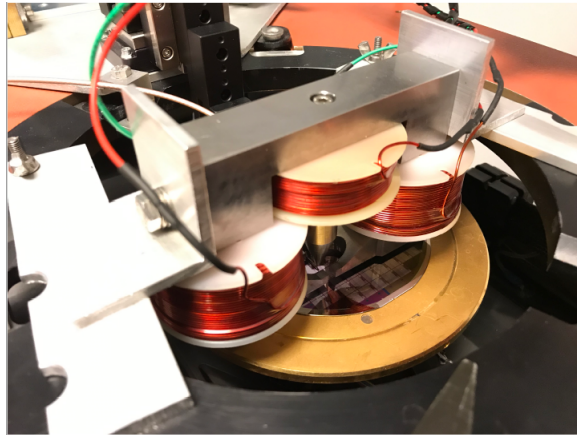


Figure 3.4: Prober.

In fig. 3.5 is possible to see the tools used to characterize the STT-MRAM device as

a sensor. In the picture we have one sourcemeter, one waveform generator, one pulse generator, one digital multimeter and one power supply. The sourcemeter and the digital multimeter are responsible of detecting the resistance, indeed the conductance is given by the ratio of the writing current over the reading voltage ($R = V_{read}/I_{write}$). The power supply provides the current that flows through the red coil and the pulse generator generates voltage pulse by means of the prober. The pulse generator and the power supply are synchronized by the waveform generator in order to be able to sweep in voltage for each step of the magnetic field and, viceversa, to sweep in magnetic field for each step of the voltage pulse (fig. 3.5).

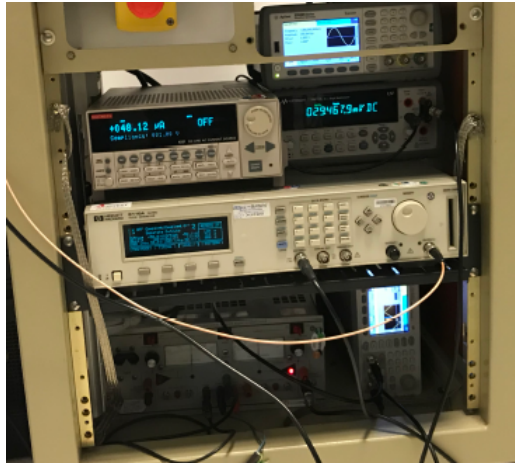


Figure 3.5: Instrumentation.

3.3 Measurements

The experiment is carried out with an STT-MRAM with 150 nm pillar diameter and the free layer thickness is of 1.3 nm. As said in the introduction, we can do two possible measurements: we can sweep the magnetic field for each voltage step or we can do the reverse, we can sweep in voltage pulse for each step of the magnetic field. As you see, in the former case the result is that we obtain the hysteresis loop as a function of the magnetic field for different voltage applied (fig. 3.6).

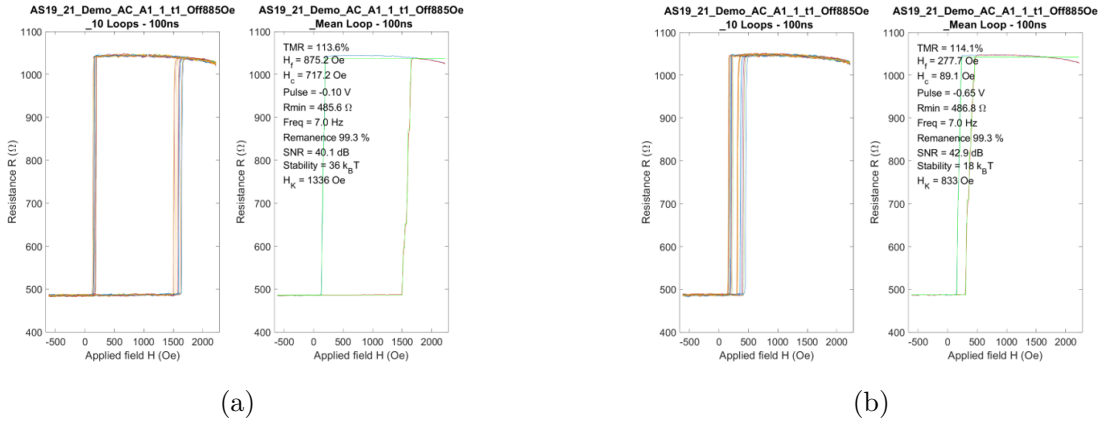


Figure 3.6: a) Hysteresis loop at -0.10 V, b) Hysteresis loop at -0.65 V.

In fig. 3.6, it is possible to see the TMR that is given by the two resistance states and the coercivity field that is half of the width of the hysteresis loop; indeed, in the figures there is written that the coercivity is 717.2 Oe (for fig. 3.6a) and 89.1 Oe (for fig. 3.6b) that corresponds to the half of the loop that is large ~ 1500 Oe for the case on the left and almost 180 Oe for the one on the right. The two plots in fig. 3.6 have different coercivity even if is the same MRAM; this happen because the device is undertake to two different applied voltages. Indeed, increasing the voltage we see that the coercivity is decreasing, this is possible to explain by considering fig. 3.7; if we see the green region, it tells us how much is wide the bistable region and so the coercive field. Indeed, if we place at a voltage of -0.10 V and we cut the graph horizontally, we see that the green region is wide and so the coercivity is half of its size. Whether we are at voltage -0.65 V we can notice that the green region is noticeably reduced, this reflects perfectly fig. 3.6.

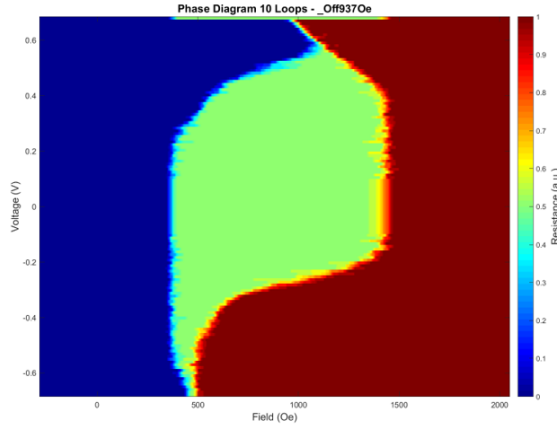


Figure 3.7: Stability Phase Diagram.

In the stability phase diagram is possible to appreciate how the switching voltages change with the external field.

The other possible experiment to do is the opposite, we can sweep with the switching voltage for each different field; we will work on this kind of measurements in order to extract the switching probability as a function of the voltage pulse.

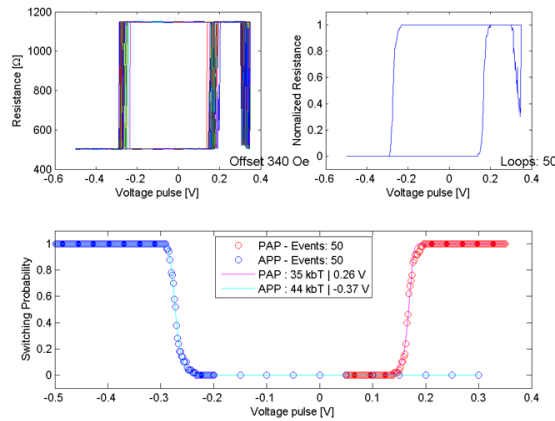


Figure 3.8: Hysteresis loop and switching probabilities measurements.

For each field we have the hysteresis loop as a function of the voltage pulse as it is possible to see in fig. 3.8 on the top right corner. The hysteresis loop built on the top left corner of fig. 3.8 is given by switching several times the junction and by making the superposition of the hysteresis loops. In this way, the switching probability is extracted

by making the histogram of the number of times that the transition from one state to the other happens. At the end, we get two different switching probabilities one relative to the negative switching voltage and the other for the positive switching voltage. For each field we extract two different switching probabilities (one for the positive switching voltage and the other for the negative switching voltage) and then we consider the voltage at which the switching probability is equal to 0.5 in both probabilities. From the experimental data is not possible to extract exactly this value, since the number of points is limited and most of the time there isn't. What we did is to make the linear interpolation of the two nearest points from that value and to extract from this the wanted values. In this way we can plot the switching voltage as a function of the external field.

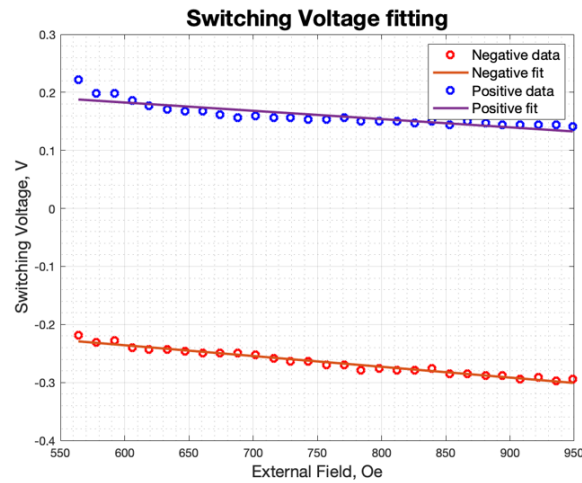


Figure 3.9: Switching voltages as a function of the magnetic field applied.

The switching voltages are decreasing with the external field so the higher is the external field and the lower will be the switching voltage. The sensitivities of these curves are $\sim 0,17mV/Oe$

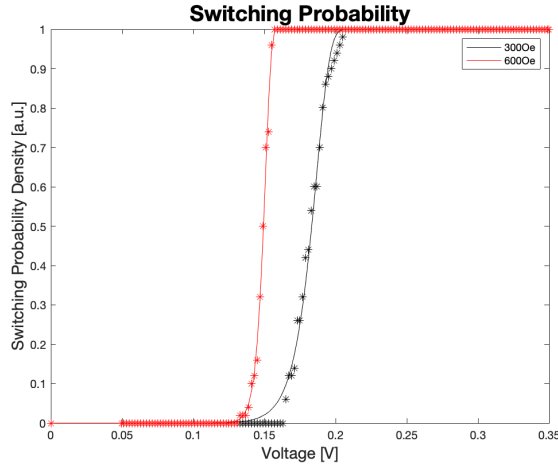


Figure 3.10: Switching probability for 300 Oe and 600 Oe.

In fig. 3.10 are plotted two different switching probabilities one for applied magnetic field of 300 Oe and the other for 600 Oe. We immediately notice that the voltage for which these two switching probabilities are equals to 0.5 changed from 0.18 V to 0.15 V respectively for 600 Oe and 300 Oe. Even the slope of the linear regions of the switching probabilities changed; indeed, the curve for 300 Oe is much less steeper than the other curve. If we translate this into the switching probability density we can study the behavior of the voltage dispersion. In 3.11 are plotted the fitting of the experimental data and it is possible to see that the FWHM changes as a function of the magnetic field.

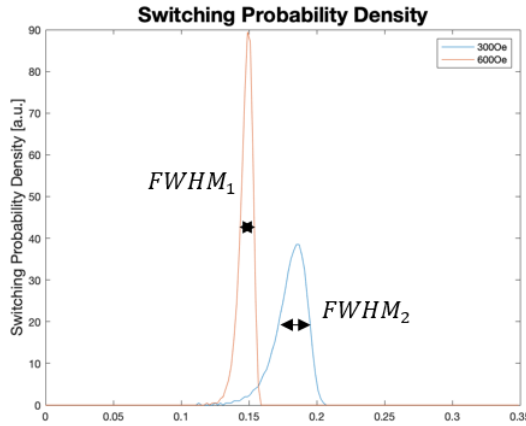


Figure 3.11: Switching probability density for 300 Oe and 600 Oe.

The experiments are in good agreement with the simulations and we can notice that the

width of the voltage dispersion is noticeably reduced and even in the switching probability density the switching voltage decreases as a function of the applied magnetic field. In the figure below there are multiple distributions that help to see this behavior.

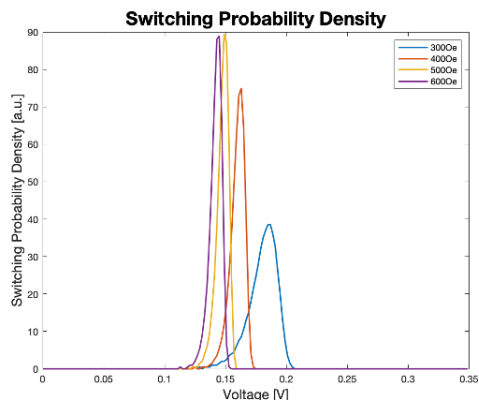


Figure 3.12: Switching probability density for 300 Oe, 400 Oe, 500 Oe and 600 Oe.

These reflects exactly the simulation in fig. 2.10. In fig. 3.13 the FWHM is represented as a function of the magnetic field, the dispersion decreases until it saturates to the value around 10 mV. This could be given by the fact that experimentally we cannot have infinite resolution for physical reasons while indeed it is possible with the simulation. So due to the finite resolution of the measurement tools, it is not possible to go beyond 10 mV of voltage dispersion.

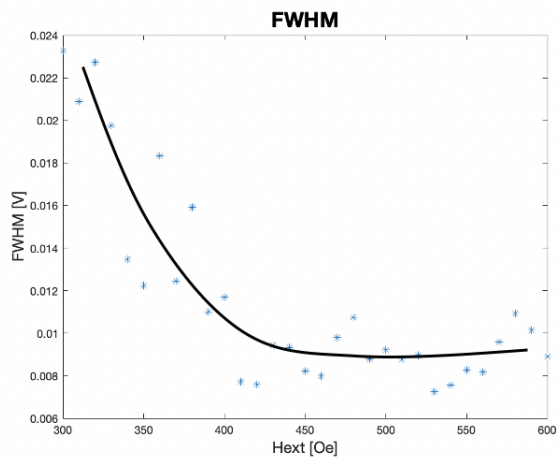


Figure 3.13: FWHM as a function of the external field.

3.4 Conclusion

We have seen that the device responds to an input magnetic field by changing the switching voltage, in our particular case the switching voltage tends to decrease with the external field applied. Another important feature is the fact that by increasing the magnetic field the voltage dispersion decreases and thus, the resolution of the detection of the magnetic field, that is in input, is higher. This is to say that we are able to recognize lower magnetic field step, if the magnetic field applied is higher. We have also seen that for very high magnetic field, the resolution of the voltage dispersion is limited by the resolution of the tools (the prober) used. Indeed, the prober has the highest resolution of 2 mV step, so is not possible to go below of that value during the measurements, this affect the resolution of the peaks.

Chapter 4

Conclusion

In this work we have seen the MRAM memory as a magnetic field sensor, in particular the application would be to use this device in order to detect possible misalignment while we are bonding two different wafers during the 3D stacking technology process. In the first part of the thesis, after a brief introduction, we started with the simulation of the device, discussing the behavior of the switching current with the applied magnetic field. Then, we extracted the sensitivity defined by the variation of the switching voltage with the magnetic field applied, so measured in mV/Oe , we concluded that the higher is this value of the sensitivity and the higher is the resolution of the device, because it enable to detect smaller details. In a first moment, we used the analytic expressions and we analysed the different behavior of the sensitivity changing different parameters; after having seen that with the TMR parameter the sensitivity was decreasing, we decided to go deepen by considering the voltage dispersion, because it's not possible that for lower TMR we have a better device since this parameter is the one that is responsible of the resolution of the two different states.

Analysing the voltage dispersion, we have seen that actually the higher is the magnetic field applied and the narrower is the voltage dispersion. Due to this, we concluded that for higher field applied we are able to detect a smaller field shift. Moving forward with the work, we have seen that if the TMR is higher, the voltage dispersion is lower leading to the conclusion that isn't true, as was for the analytic expression, that for lower TMR we obtain a better device, instead is totally the opposite.

Besides, after having explained the role of the magnetic element and the field generated by it, we introduced the lateral and the vertical sensitivity that are the one responsible of the misalignment detection both in the horizontal and in the vertical direction respectively and we have seen that thanks to the difference of the switching voltages it is possible to enhance the slope of the sensitivity. We have seen that by placing in different positions multiple magnetic elements and MRAM devices we obtained higher resolution. For the lateral sensitivity an higher resolution is obtained when the sensor is sensitive for higher horizontal displacement, while for vertical sensitivity is increased when the sensor is able to detect further vertical displacements of the magnetic element. This two design

parameters can be improved by the use of different geometries enhancing this physical magnitudes. In the experimental part we have seen the two different methods that we use for measurements and the experiments confirm that the higher is the magnetic field and the higher is the resolution with which we can detect the step field. However, the resolution is even limited by the measurement tools that we are using. The work of this thesis is arrived until this point for time reasons, but it is possible to continue with the project by implementing, from the experimental point of view, the solution we have find in the simulation; so it is possible to test the behavior of the sensitivity of the MRAM with different parameters, then it would be interesting seeing how does the voltage dispersion changes with the TMR. Besides, it must continue with the definition of the lateral and vertical sensitivity from an experimental point of view. After that, it could be interesting to first simulate and then to test different geometries by using different marker's structure in order to generate the peaks sharper and, in this way, it could be possible to increase the resolution of the system.

Bibliography

- [1] Robert Beringer and Mark A. Heald. “Electron Spin Magnetic Moment in Atomic Hydrogen”. In: *Phys. Rev.* 95 (6 Sept. 1954), pp. 1474–1481. DOI: [10.1103/PhysRev.95.1474](https://doi.org/10.1103/PhysRev.95.1474). URL: <https://link.aps.org/doi/10.1103/PhysRev.95.1474>.
- [2] Bernard Dieny, Ronald B Goldfarb, and Kyung-Jin Lee. *Introduction to magnetic random-access memory*. Hoboken, NJ: Wiley-IEEE Press, 2017. URL: <http://cds.cern.ch/record/2240140>.
- [3] Sebastien Mermoz. “Self-assembly assisted by capillarity and direct bonding”. Theses. Université Grenoble Alpes, June 2015. URL: <https://tel.archives-ouvertes.fr/tel-01290184>.
- [4] N. Perrissin et al. *Highly thermally stable sub-20nm magnetic random-access memory based on perpendicular shape anisotropy*. 2018. arXiv: [1803.02663](https://arxiv.org/abs/1803.02663) [[cond-mat.mtrl-sci](https://arxiv.org/abs/1803.02663)].
- [5] Clément Sart. “Numerical and Experimental Investigations on Mechanical Stress in 3D Stacked Integrated Circuits for Imaging Applications”. Theses. Université Grenoble Alpes, Dec. 2019. URL: <https://tel.archives-ouvertes.fr/tel-02517015>.
- [6] H. Sato et al. “Properties of magnetic tunnel junctions with a MgO/CoFeB/Ta/CoFeB/MgO recording structure down to junction diameter of 11nm”. In: *Applied Physics Letters* 105.6 (2014), p. 062403. DOI: [10.1063/1.4892924](https://doi.org/10.1063/1.4892924). eprint: <https://doi.org/10.1063/1.4892924>. URL: <https://doi.org/10.1063/1.4892924>.
- [7] Tomohiro Taniguchi. “An analytical computation of magnetic field generated from a cylinder ferromagnet”. In: *Journal of Magnetism and Magnetic Materials* 452 (2018), pp. 464–472. ISSN: 0304-8853. DOI: <https://doi.org/10.1016/j.jmmm.2017.11.078>. URL: <http://www.sciencedirect.com/science/article/pii/S0304885317321418>.
- [8] L. Tillie et al. “Data retention extraction methodology for perpendicular STT-MRAM”. In: *Electron Devices Meeting (IEDM), 2016 IEEE International*. San Francisco, United States, Dec. 2016. DOI: [10.1109/IEDM.2016.7838492](https://doi.org/10.1109/IEDM.2016.7838492). URL: <https://hal.archives-ouvertes.fr/hal-01718116>.
- [9] A. A. Timopheev et al. “Respective influence of in-plane and out-of-plane spin-transfer torques in magnetization switching of perpendicular magnetic tunnel junctions”. In: *Phys. Rev. B* 92 (10 Sept. 2015), p. 104430. DOI: [10.1103/PhysRevB.92.104430](https://doi.org/10.1103/PhysRevB.92.104430). URL: <https://link.aps.org/doi/10.1103/PhysRevB.92.104430>.